

AD-A264 200



RL-TR-92-340  
In-House Report  
December 1992

**DTIC**  
**S** **ELECTE** **D**  
**C**  
MAY 12 1993



(2)

# PHOTOREFRACTIVE INTEGRATORS AND CORRELATORS

George A. Brost

*APPROVED FOR PUBLIC RELEASE; DISTRIBUTION UNLIMITED.*

This effort was funded totally by the Laboratory Director's fund.

93 5 11 30 2

93-10455

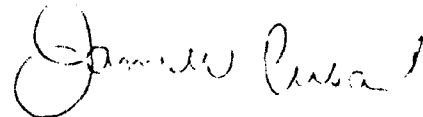


Rome Laboratory  
Air Force Materiel Command  
Griffiss Air Force Base, New York

This report has been reviewed by the Rome Laboratory Public Affairs Office (PA) and is releasable to the National Technical Information Service (NTIS). At NTIS it will be releasable to the general public, including foreign nations.

RL-TR-92-340 has been reviewed and is approved for publication.

APPROVED:



JAMES W. CUSACK, Chief  
Photonics & Optics Division  
Surveillance & Photonics Directorate

FOR THE COMMANDER:



JAMES W. YOUNGBERG, LtCol, USAF  
Deputy Director  
Surveillance & Photonics Directorate

If your address has changed or if you wish to be removed from the Rome Laboratory mailing list, or if the addressee is no longer employed by your organization, please notify RL (OCPA) Griffiss AFB NY 13441-5700. This will assist us in maintaining a current mailing list.

Do not return copies of this report unless contractual obligations or notices on a specific document require that it be returned.

# REPORT DOCUMENTATION PAGE

Form Approved  
OMB No. 0704-0188

Public reporting burden for this collection of information is estimated to average 1 hour per response, including the time for reviewing instructions, searching existing data sources, gathering and maintaining the data needed, and completing and reviewing the collection of information. Send comments regarding this burden estimate or any other aspect of this collection of information, including suggestions for reducing this burden, to Washington Headquarters Services, Directorate for Information Operations and Reports, 1215 Jefferson Davis Highway, Suite 1204, Arlington, VA 22202-4302, and to the Office of Management and Budget, Paperwork Reduction Project (0704-0188), Washington, DC 20503.

1. AGENCY USE ONLY (Leave Blank)		2. REPORT DATE December 1992		3. REPORT TYPE AND DATES COVERED In-house Oct 90 - Sep 92	
4. TITLE AND SUBTITLE PHOTOREFRACTIVE INTEGRATORS AND CORRELATORS				5. FUNDING NUMBERS PE - 61161F PR - LDFP TA - 02 WC - R1	
6. AUTHOR(S) George A. Brost					
7. PERFORMING ORGANIZATION NAME(S) AND ADDRESS(ES) Rome Laboratory (OCPA) 25 Electronic Parkway Griffiss AFB NY 13441-4515				8. PERFORMING ORGANIZATION REPORT NUMBER	
9. SPONSORING/MONITORING AGENCY NAME(S) AND ADDRESS(ES) Rome Laboratory (OCPA) 25 Electronic Parkway Griffiss AFB NY 13441-4515				10. SPONSORING/MONITORING AGENCY REPORT NUMBER RL-TR-92-340	
11. SUPPLEMENTARY NOTES Rome Laboratory Project Engineer: George A. Brost/OCPA (315) 330-7669 This effort was funded totally by the Laboratory Director's fund.					
12a. DISTRIBUTION/AVAILABILITY STATEMENT Approved for public release; distribution unlimited.				12b. DISTRIBUTION CODE	
13. ABSTRACT (Maximum 200 words) The use of photorefractive crystals as optically addressed time integrating spatial light modulators in acousto-optic signal processing applications was examined. Non-stationary recording techniques of alternating electric fields and moving fringe patterns were investigated in detail. A finite difference technique was used to model grating formation characteristics. Photorefractive $\text{Bi}_{12}\text{SiO}_{20}$ and $\text{BaTiO}_3$ crystals were tested experimentally in an adaptive acousto-optic processor. These results demonstrated the feasibility of using photorefractives for such applications.					
14. SUBJECT TERMS photorefractive, acousto-optic processor				15. NUMBER OF PAGES 88	
				16. PRICE CODE	
17. SECURITY CLASSIFICATION OF REPORT UNCLASSIFIED	18. SECURITY CLASSIFICATION OF THIS PAGE UNCLASSIFIED	19. SECURITY CLASSIFICATION OF ABSTRACT UNCLASSIFIED	20. LIMITATION OF ABSTRACT U/L		

## CONTENTS

ACKNOWLEDGEMENT	1
1. INTRODUCTION	2
2. BACKGROUND	4
2.1 Acousto-optic Correlation	4
2.2 Photorefractive integration	6
2.3 Holographic readout	7
2.4 Photorefractive crystal characteristics	9
3. NONSTATIONARY RECORDING TECHNIQUES	13
3.1 AC Fields	16
3.1.1 Numerical method	16
3.1.2 Numerical results	21
3.1.3 Discussion	36
3.1.4 Experimental results	40
3.1.5 AC Field frequency dependence	44
3.2 Moving Gratings	51
3.2.1 Small modulation theory	51
3.2.2 Numerical results	52
4. PHOTOREFRACTIVE CHARACTERIZATION	64
4.1 BSO	64
4.2 Barium Titanate	68
5. ACOUSTO-OPTIC CORRELATION & APPLICATION	70
5.1 Photorefractive acousto-optic correlation	70
5.2 Acousto-optic adaptive processing	73
6. SUMMARY	78
REFERENCES	79

## ACKNOWLEDGEMENTS

The collaboration and contributions of others is gratefully acknowledged. Experimental ac field data on BTO was taken by James Millerd. Acousto-optic adaptive processing experiments were conducted under the technical guidance and participation of Chris Keefer.

Accession For	
CRIS CRA&I	<input checked="checked" type="checkbox"/>
DTIC TAB	<input type="checkbox"/>
Unannounced	<input type="checkbox"/>
Justification	
By	
Distribution /	
Availability Codes	
Dist	Avail and/or Special
A-1	

## I. INTRODUCTION

In the photorefractive effect the photo-generation and redistribution of charges among traps, due to nonuniform illumination of light, results in the formation of a space-charge field. Through the electro-optic effect, a volume holographic phase grating is formed. The dynamics of the photorefractive grating formation and erasure is equivalent to performing a time integration. The photorefractive method of time-integration is attractive for optical signal processing requiring an optically addressed spatial light modulator. Photorefractive integration also has the advantages of providing parallel optical output, bias-free operation, and high resolution[1]. The use of photorefractives for time integration was first suggested by Psaltis *et al.*[1] and more recently by Montgomery[2].

This report examines the use of photorefractive crystals as time-integrating elements for optical signal processing. Particular emphasis is directed towards the application to acousto-optic adaptive processing. Section 2 provides a background on photorefraction and the application to signal processing. Section 3 presents new theoretical and experimental investigations on nonstationary photorefractive recording techniques in sillenite crystals. The ac field and moving grating techniques appear attractive for signal processing applications in  $\text{Bi}_{12}\text{SiO}_{20}$  (BSO), but there has not been available an accurate means of predicting the performance characteristics. Section 4 describes experimental investigations of photorefractive characteristics related to implementation as

integrators. BSO is emphasized as a candidate material. Barium titanate is considered also. Section 5 describes the use of a photorefractive integrator in an acousto-optic adaptive processing application.

## 2. BACKGROUND

This section provides a background on photorefraction and the application of the photorefractive effect to acousto-optic signal processing.

### 2.1 Acousto-Optic Correlation

Acousto-optic correlation is an important function of optical signal processing. A time integrating acousto-optic correlator is shown schematically in Figure 1. Here one signal,  $s(t)\cos(\omega_c(t-D_s))$  is applied to the acoustic input of the Bragg cell and the other,  $r(t)\cos(\omega_c(t-D_r))$ , is modulated directly onto the laser source. If a time integrating element is placed in the image plane of the Bragg cell, then the integrated optical exposure  $I(x)$  will contain the correlation function between  $s(t)$  and  $r(t)$ .

$$I(x) = I_0[1+m\sin(\omega_c(D_r+D_s+x/v)) \int r(t+D_r)s(t-D_s-x/v)dt. \quad (1)$$

Here  $v$  is the acoustic velocity of the AO cell,  $D_r$  and  $D_s$  are time delays, and  $m$  is a modulation term determined by the diffraction efficiency of the AO cell and the modulation depth imposed on the laser source.

Usually a photodetector array is used to read this exposure and extract the correlation values. The processing is done in the electronic domain. Alternatively, a photorefractive material could be used to perform the integration. In this case the correlation would be read out optically.



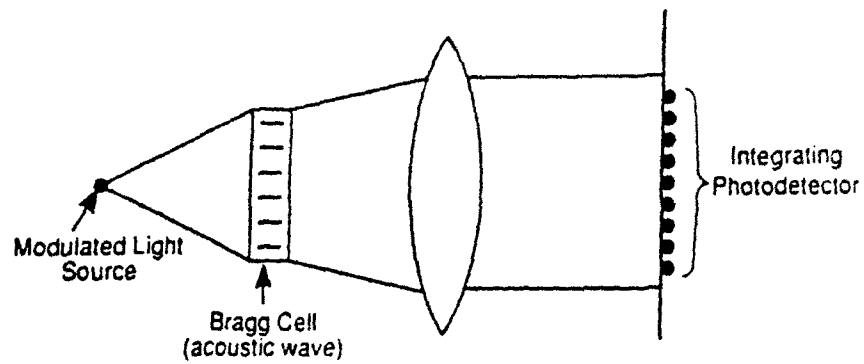


Figure 1. Acousto-optic time integrating correlator.

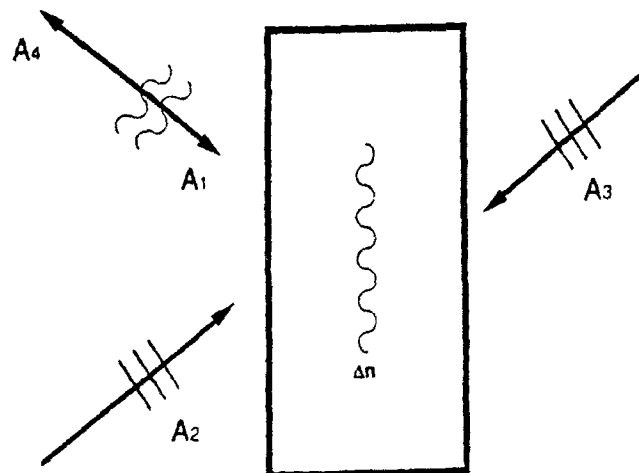


Figure 2. Schematic of photorefractive detector.

## 2.2 Photorefractive integration

The basic physical model of photorefraction has been well established. The process involved is a light-induced redistribution of charges among traps. The resulting space-charge field then modulates the refractive index through the linear electro-optic effect. The response of the photorefractive material to a spatially modulated light intensity pattern is well described by a set of nonlinear differential equations.

The basic configuration for utilizing the photorefractive effect is shown schematically in Figure 2. The interference of two coherent write beams, which may be modulated both spatially and temporally, give rise to an intensity distribution within the crystal given by:

$$I(x,t) = I_0 + I_1(x,t)\exp(iKx) \quad (2)$$

where  $K$  is grating spatial frequency of the optical carrier, determined by the crossing angle of the two write beams. Provided that the spatial variations of  $I_1(x,t)$  are slow compared to the grating frequency and the magnitude of  $I_1$  is much less than  $I_0$  (small modulation approximation), the space charge field formed in the crystal is[1]

$$E_{SC}(x,t) = E_1 \exp(iKx + \phi) \int_0^t \exp[(t-t')/\tau_g] I_1(x,t')/I_0 dt' \quad (3)$$

where  $E_1$  and  $\tau_g$  are complex and depend on material parameters and external conditions. This response may be approximated as[1]

$$E_{SC}(x,t) \approx E_1 \exp(iKx + \phi) \int_{t-\tau_g}^t |I_1(x,t')/I_0| dt' \quad (4)$$

The space charge field, therefore, reflects a running average of the light intensity pattern. For an exposure given by equation (1) the space charge field is

$$E_{SC}(x) = E_1 m \sin(w_c(x/v + \phi)) \int |r(t+D_r)s(t-D_s-x/v)| dt \quad (5).$$

The photorefractive phase grating therefore contains the desired correlation with spatial carrier of frequency  $w_c/v$ .

### 2.3 Holographic readout

Through the electro-optic effect, the photorefractive space charge field modulates the refractive index to create a holographic phase grating. The magnitude of the phase grating is given by

$$\Delta n = 1/2 n_0^3 r_{eff} E_{SC} \quad (6)$$

where  $n_0$  is the index of refraction  $r_{eff}$  is the effective electro-optic tensor component. This grating may be read out with a plane wave read beam via Bragg diffraction, as indicated in Fig. 2. The wavelength of the read beam need not be the same as the write beams. The diffraction efficiency  $\eta$ , defined as the

ratio of the diffracted intensity to the incident intensity, is given by

$$\eta = \exp(-\alpha l) \sin^2(\pi \Delta n l / \lambda) \quad (7)$$

where  $\alpha$  is the absorption coefficient,  $l$  is the interaction length, and  $\lambda$  is the wavelength. The amplitude of the diffracted read beam is proportional to  $E_{SC}$ , and therefore, the correlation function. This read beam may be detected with a photodiode array.

For acousto-optic adaptive signal processing applications which are of interest to Rome Laboratory an alternate holographic readout approach is appropriate. In this application the magnitudes of  $r(t)$  and  $s(t)$  are slowly varying in time and both the magnitude and phase of the hologram is required. This can be obtained with a heterodyne detection of the readout. Here the zeroth order and first order readout beams are imaged onto an AO Bragg cell, whose acousto optic spatial frequency is matched to the photorefractive spatial frequency. The zeroth order beam is Bragg tuned to the AO cell so that the first order AO Bragg diffraction overlaps the photorefractive holographic diffracted beam. The detected signal will then contain a dc term plus a heterodyne component with a frequency equal to that of the drive frequency of the Bragg cell. The magnitude of the heterodyne signal will be proportional to the magnitude of the space charge field, and therefore the correlation term. The phase of the detected signal, relative to a reference input, will depend upon the physical location of the holographic grating inside the photorefractive crystal, which in turn depends upon the phase

difference between  $r(t)$  and  $s(t)$ .

## 2.4 Photorefractive crystal characteristics

In this section we highlight some of the key photorefractive crystal characteristics, relevant to acousto-optic signal processing. A more detailed review of photorefractive properties can be found in references 3 and 4.

The diffraction efficiency is a key characteristic, directly related to the system signal to noise ratio and its dynamic range. As seen by equations (6) and (7), the diffraction efficiency depends upon the magnitude of the induced space charge field and on the electro-optic coefficient.

We consider first the space charge field. Its magnitude will depend primarily on the external conditions, such as applied electric field and grating period. Under the anticipated imaging conditions the crystals will be used in the long grating period regime, with grating periods on the order of 10 to 50  $\mu\text{m}$ . At these long grating periods the space charge field, in the absence of an applied electric field, is diffusion limited, and is given by

$$E_{SC} \approx mE_D = m2\pi k_B T / (\Lambda q) \quad (8)$$

where  $\Lambda$  is the grating period  $q$  is the electronic charge,  $k_B$  is Boltzman's constant, and  $T$  is the temperature, and  $m$  is the modulation depth of the light intensity pattern. For a 20  $\mu\text{m}$  grating period  $E_D$  is only about 80 V/cm. The space charge field

can be significantly increased by the application of the electric field,  $E_A$ . For a dc applied field the magnitude of the space charge field is then

$$E_{SC} \approx mE_A \quad (9)$$

Typical applied field strengths are 2-10 KV/cm. Further enhancements can be realized through nonstationary recording techniques of moving gratings or applied alternating electric fields[3,5]. With these techniques the space charge field can be enhanced by a factor  $R$  over that of a dc field alone. The enhancement factor  $R$  depends upon crystal parameters such as the mobility lifetime product, as well as the applied voltage. A typical value of  $R$  for sillenite crystals is about 3 to 4. This makes the nonstationary recording techniques very attractive, and will be discussed in more detail in section 3.

The diffraction efficiency also depends upon the magnitude of the electro-optic coefficient. The electro-optic coefficients of some representative crystals are shown in Table 1. Although those crystals with large electro-optic coefficients offer the highest diffraction efficiency, this characteristic may be offset by time response considerations.

The time constant for the buildup of the photorefractive grating is also an important characteristic. The time required to record a grating depends upon the charge generation and transport processes, and is inversely proportional to the light intensity.

Three separate classes of photorefractive materials have dominated -- ferroelectric oxides, cubic oxides (sillenites) and

semi-insulating compound semiconductors. The ferroelectric oxides such as barium titanate ( $\text{BaTiO}_3$ ) have large electro-optic coefficients, leading to large diffraction efficiencies. On the other hand these crystals have small charge carrier mobilities and large dielectric constants, which cause poor sensitivity. The sillenites, such as  $\text{Bi}_{12}\text{SiO}_{20}$  (BSO) have much smaller electro-optic coefficients, similar mobilities, and smaller dielectric constants, and are more sensitive than the ferroelectrics. The semi-insulating semiconductors, such as GaAs and InP, have small electro-optic coefficients, but large mobilities. A comparison of photorefractive properties is shown in Table 1.

BSO was chosen as a candidate photorefractive integrator which could be immediately transitioned into the acousto-optic adaptive processor. BSO is widely available commercially, and is also grown at Rome Laboratory. BSO has good sensitivity at 514 nm, the current design wavelength of the adaptive processor which uses a liquid crystal light valve as the integrating element, and is readily available in widths greater than 1 cm. Although the electro-optic coefficient is small ( $\approx 4 \text{ pm/V}$ ), BSO has the necessary response time of about 10-100 msec.

TABLE 1. Properties of some photorefractive crystals

PARAMETER	UNITS	BaTiO <sub>3</sub>	BSO	GaAs
wavelength range	$\mu\text{m}$	0.4 - 0.8	0.45-0.65	1.0-1.5
dielectric constant		3700 ( $\epsilon_{11}$ ) 135 ( $\epsilon_{33}$ )	56	13
EO coefficient	pm/V	1640 ( $r_{42}$ ) 90 ( $r_{33}$ ) 24 ( $r_{13}$ )	4 ( $r_{41}$ )	1.4 ( $r_{41}$ )
mobility	$\text{cm}^2/\text{V-s}$	0.2	0.1	5000
photoconductivity	$\text{cm}^2/\text{V}$	$10^{-10}$	$10^{-7}$	$10^{-4}$
response time (at 100 mW/cm <sup>2</sup> )	msec	1-10K	10-100	10-100

Recently, a new class of photorefractive structures have been developed which take advantage of the high nonlinearities possible in multiple quantum well structures[5,6]. Two geometries have emerged, the so called perpendicular and parallel geometry according to whether the electric field is applied perpendicular or parallel to the quantum well layers. High diffraction efficiencies have been demonstrated in the MQWs. The MQWs have the advantages of fast response times, operation at laser diode wavelengths, and low voltage biasing requirements. These devices are not yet commercially available, and were not tested in this effort.



### 3. NONSTATIONARY PHOTOREFRACTIVE RECORDING TECHNIQUES

Enhancements in the photorefractive effect can be achieved in sillenite crystals such as  $\text{Bi}_{12}\text{SiO}_{20}$  (BSO) and  $\text{Bi}_{12}\text{TiO}_{20}$  (BTO) by the use of nonstationary external conditions.[7-11] The ac field[8-10] and moving grating[7,10,11] techniques can significantly increase the magnitude of the space charge field over that which would result from the application of a dc field alone. These enhancement techniques also maximize the component of the index grating at  $90^\circ$ . The high diffraction efficiency and phase characteristics of the grating make these nonstationary recording techniques attractive for device applications. However, the large enhancements have been achieved only with weak signal beams. For modulation index,  $m$ , greater than about 0.02, the performance apparently falls off significantly with increasing  $m$ . [7,12,13] This behavior is in contrast to the mild influence of modulation index on the gain coefficient under stationary recording conditions.[14] An understanding of the nonstationary recording behavior is important when considering the limitations of these devices.

The usual solutions of the nonlinear material equations utilize the small modulation approximation to obtain analytical expressions. These linearized solutions have provided good agreement with experiment for stationary recording conditions even up to  $m \approx 1$ . For nonstationary recording conditions it is necessary to include higher harmonics when the small  $m$  approximation is not strictly valid.

Some progress had been made in understanding the modulation effects with nonstationary recording conditions, primarily for moving gratings.[7,14-17] Refregier et al.[7] were able to obtain partial agreement with their experimental data for moving gratings by applying a second order perturbation. Swinburne et al.[14] and Au and Solymar[15,16] obtained numerical steady state solutions which predicted a gain saturation, but these effects were not examined in any detail. Swinburne et al.[14] derived some approximate results for external conditions of an applied square wave ac field which predicted the existence of an upper limit to the enhancement of the space charge field. Their model provides an analytical expression for the local space charge field as a function of modulation index, but does not have the proper grating period dependence.[13]

In this section we examine in more detail the modulation dependence under nonstationary recording conditions of applied ac fields and moving gratings. The goal is to provide the necessary understanding to be able to model and predict the performance characteristics of photorefractive integrators. A finite difference method was developed to model the photorefractive grating formation in BSO and BTO crystals, and is described in detail. The influence of modulation index on the magnitude, spatial distribution, and temporal evolution of the space charge field are examined. The space charge field magnitude is shown to be limited to the order of the applied electric field and that the dependence of the space charge field on modulation index can be predicted from crystal parameters over a large range of recording conditions. The numerical

results are generalized to other crystal parameters and external conditions by finding analytical equations which approximate the numerical solutions. The ac field case is examined in section 3.1, where the numerical method is also described. In section 3.2 the analysis is applied to moving gratings.

### 3.1 AC Fields

In the ac field technique the external alternating electric field is applied with a time period  $T_{ac}$  which satisfies the conditions  $\tau_g \gg T_{ac} \gg \tau_R$ , where  $\tau_g$  is the grating formation time constant and  $\tau_R$  is the free carrier lifetime. The phase grating is then  $90^\circ$  phase shifted with respect to the fringe pattern. The magnitude of the space charge field depends on the form of the ac field. A square-wave alternating field is much more efficient than a sinusoidal alternating field of the same amplitude. The magnitude of space charge field for the square-wave case is given by[8]

$$E_{SC} = m \frac{E_D}{(1+K^2 l_s^2)} \frac{1 + K L_E E_A / [E_D (1+K^2 L_D^2)]}{1 + K^2 L_E r_E / [(1+K^2 L_D^2) (1+K^2 l_s^2)]} \quad (10)$$

where  $E_D = K k_B T / q$ ,  $L_E = \mu \tau_R E_A$  is the drift length,  $L_D = (D \tau_R)^{1/2}$  is the diffusion length,  $l_s = (\epsilon_0 k_B T / q^2 N_e)^{1/2}$ , and  $r_E = \epsilon_0 E_A / q N_e$ . The peak magnitude of the space-charge field varies as  $\mu \tau_R N_e$ . For sillenite crystals this value ( $E_{SC}/m$ ) is approximately  $4E_A$ .

An important feature of nonstationary recording is that the grating formation time constant is real for the square wave ac field technique, and is equal to the time constant for a dc applied electric field[9,10].

#### 3.1.1 Numerical Method

In order to determine the characteristics of the space-charge field under conditions of high modulation the grating formation

was modeled with a finite difference scheme. The microscopic space-charge field was calculated under the assumptions that the spatial symmetry of the grating formation was one dimensional and periodic in the grating vector direction. With these assumptions it was only necessary to calculate the charge redistribution over one grating period of length, which was divided into  $N$  cells. The electric field, and free carrier, carrier current, and charge densities were determined for each cell. The current was allowed to flow for a time period  $\delta t$  and the change in the free carrier concentration was determined by the continuity equation. The distribution of charge among free carriers and traps was then recalculated and the other quantities updated.

We start with the material equations which describe the redistribution of charges among traps. These equations are:

$$dN_1/dt = -(S_1 I + \beta_1)N_1 + \gamma_1(N_{1T} - N_1)N_h \quad (11)$$

$$dN_h/dt = -dN_1/dt \quad (12)$$

$$\partial N_h/\partial t = dN_h/dt - \nabla \cdot j_h \quad (13)$$

$$j_h = \mu_h N_h E - D \nabla N_h, \quad (14)$$

$$\nabla \cdot E = \rho/\epsilon\epsilon_0, \quad (15)$$

where  $N_{1T}$  is the total number density of photorefractive centers,  $N_1$  is the number density of unionized charge donors,  $N_h$  is the number density of free carriers (our equations are written for positively charged free carriers),  $j_h$  is the free carrier current density,  $S_1$  is the photon-absorption cross section,  $\gamma_1$  is the recombination coefficient,  $\beta_1$  is the thermal

ionization rate,  $\mu_h$  is the carrier mobility,  $D$  is the diffusion coefficient given by  $D = \mu_h k_B T / q$ ,  $E$  is the electric field which includes both the applied field  $E_A$  and the space charge field  $E_{SC}$ ,  $\epsilon$  is the dielectric constant,  $\epsilon_0$  is the permittivity of free space,  $\rho$  is the charge density, and  $I$  is the laser intensity.

The light intensity pattern is assumed to be spatially periodic and may be time-varying. We assume a sinusoidal intensity pattern with the following form.

$$I(x,t) = I_0(t) \{1 + m \sin[Kx - \phi(t)]\}, \quad (16)$$

where  $I_0$  is the total intensity,  $m$  is the modulation index,  $K$  is the grating wave number, and  $\phi$  is the time dependent phase shift. For two vertically polarized input waves of intensities  $I_S$  and  $I_R$ ,

$$m = 2\beta^{1/2} / (\beta + 1), \quad (17)$$

where  $\beta = I_R / I_S$ .

The distribution of charges among the traps and free carrier concentrations in each cell were determined from the rate Eqs. (11,12), subject to the constraint of charge conservation

$$N_{1i} + N_{hi} - N_{oi} = 0, \quad (18)$$

where  $i$  refers to the  $i$ th cell, and  $N_{oi} = N_{1di} + N_{hdi} + \Delta N_{hi}$ .

Here  $N_{1di}$  and  $N_{hdi}$  are the initial dark concentration levels

before the light was turned on and  $\Delta N_{hi}$  is the net gain of free carriers in the  $i$ th cell due to the nonuniform current flow. Since  $\Delta N_{hi}$  changes at each time step, the constraint given by Eq. (18) also varies at each time iteration. A fourth order Runge Kutta technique was used to integrate the rate equations.

The free carrier current was then determined for each cell from Eq. (14). The photoinduced space charge field could be determined by combining the one dimensional continuity equation with Poisson's equation to give[18]

$$E_{SC}(x,t) = -q/\epsilon\epsilon_0 \int_0^t j_h(x,t) dt + G(t), \quad (19)$$

where  $G(t)$  is determined from the boundary condition of the constraint of a constant applied voltage given by

$$-\int_0^L E(x,t) dx = V, \quad (20)$$

where  $E(x,t) = E_{SC}(x,t) + E_A(t) = E_{SC}(x,t) - V(t)/L$  is the total electrostatic field and  $L$  is the crystal length. With the assumption of periodicity this means that

$$\int_{x'}^{x'+L} E_{SC}(x,t) dx = 0. \quad (21)$$

The space charge field was determined by applying Eqs. (19-21).

The one dimensional continuity equation was used in the

following form to determine the change in the free carrier concentration in the  $i$ th cell:

$$\Delta N_{hi} = -(\nabla \cdot j_{hi}) \delta t. \quad (22)$$

The results from Eq. (22) were used to update the charge conservation constraint given by Eq. (18) in the solution of the rate equations on the next iteration.

These calculations provided a temporal evolution of the space charge field as well as other quantities such as free carrier and charge densities. Calculations were carried out to an approximate steady state condition, typically to about 10 - 20 grating time constants. The number of cells,  $N$ , into which the grating was divided, depended upon the degree of the nonlinearity. At high modulation, a small  $N$  would result in an unrealistic magnitude of some of the higher harmonic components. The value for  $N$  was chosen to meet the requirement that high frequency oscillations in the spatial distribution of the space charge field be well behaved. Consequently  $N$  ranged from as low as 20 for small modulation calculations to as high as 400 for some large modulation cases. For stability, the time step at each iteration was required to be less than the free carrier lifetime and characteristic transport times. This numerical approach calculated the full space charge field within the resolution of the element size. The magnitude and phase of the harmonic components were determined by Fourier decomposition of the calculated space charge field.



### 3.1.2 Numerical Results

As the numerical method used here was very computer intensive it was practical to calculate grating formations only for a limited, but representative set of parameters. Calculations for BTO assumed  $\mu\tau = 6.8 \times 10^{-8} \text{ cm}^2/\text{V}$ ,  $N_e = 3 \times 10^{16} \text{ cm}^{-3}$ , and  $\epsilon = 47$ . These values correspond to those reported by Millerd et al.[13], which allowed comparison of the numerical calculations with their experimental results. For BSO we used  $\epsilon = 56$ ,  $N_e = 1 \times 10^{16} \text{ cm}^{-3}$ , and  $\mu\tau$  ranged from  $6.25 \times 10^{-8}$  to  $6.25 \times 10^{-7} \text{ cm}^2/\text{V}$ . A range of enhancement characteristics were examined through variations in the grating period, applied field, and  $\mu\tau$ . At small  $m$  the numerical results were in good agreement with the linearized theory. We note that the space-charge field amplitude exhibited a small modulation at two times the ac field frequency, and the spatial phase of the fundamental component exhibited a small oscillation about a  $90^\circ$  phase shift with a frequency of the applied ac field. These effects are discussed in detail below. The modulation dependent results reported here reflect the time averaged amplitude and phase.

The large signal effect, in which the gain decreases significantly at large modulation is demonstrated in Figure 3. Here we plot the magnitude of the imaginary part of the fundamental component of the space charge field ( $E_1$ ) normalized with respect to the modulation index as a function of beam ratio ( $\beta$ ) for different applied electric field strengths in BTO. We note that the fundamental component remained  $90^\circ$  phase shifted from the light intensity pattern for all beam ratios. According

to the linearized theory,  $E_1/m$  should be constant, independent of the beam ratio. The magnitudes of the calculated space charge fields fell off from the large beam ratio values and declined to a magnitude on the order of the applied field at  $\beta = 1$ .

In Figure 4 we plot these results as  $f(m)$  vs  $m$ . Here  $f(m)$  is the correction function introduced by Refregier et al.[7] which relates the magnitude of the fundamental component of the space charge field to the modulation index:

$$E_1(m) = f(m)E_0, \quad (23)$$

where  $E_0$  is the maximum imaginary part of the fundamental component of the space charge field that can be obtained, and was determined from  $E_1/m$  calculated for very small  $m$ . In the linear-in-modulation approximation  $f(m) = m$ . However, as the numerical results show, the value of  $E_1$  increased sublinearly with  $m$ .

It is useful to consider the functional form of  $f(m)$ . The numerical results could be described quite well by the equation:

$$f(m) = 1/a[1 - \exp(-am)]\exp(m). \quad (24)$$

This function is similar to the correction function Refregier et al.[7] determined phenomenologically for moving gratings. The solid lines for the results shown in Figure 4 are fits of Eq. (24) to the calculated  $f(m)$ . Similar results were obtained for other calculations which reflected a range of crystal parameters

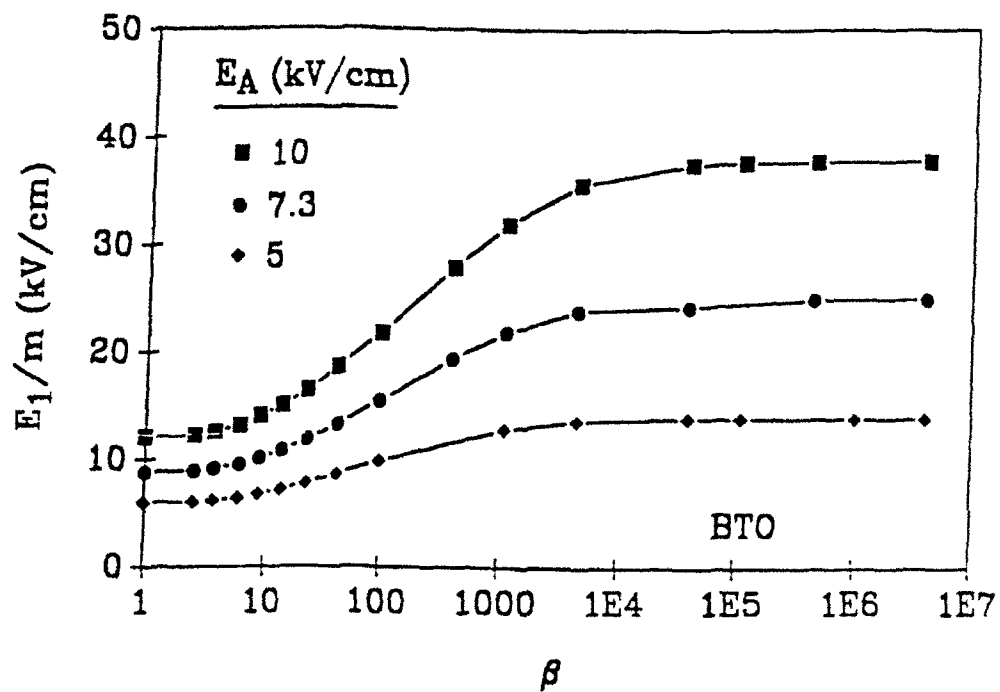


Figure. 3. Normalized space charge field vs beam ratio for different applied square-wave ac field strengths in BTO.

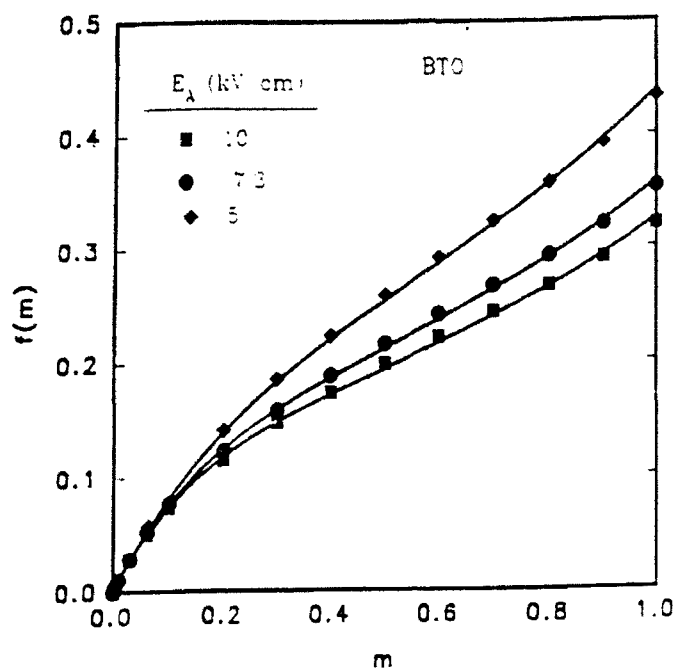


Figure 4. Calculated correction function vs modulation index for different applied square-wave ac field strengths in BTO. The solid line is a fit of the numerical results to the equation  $f(m) = 1/a[1-\exp(-am)]\exp(m)$ . The values of  $a$  determined from the fits were 8.35, 7.6, and 6.2.

and recording conditions. Some examples are shown in Fig. 5. The lines are a fit of Eq. (24) to the numerical results. This equation provided a good description of the results over a wide range of saturation characteristics. At long grating periods the linearized theory predicts  $E_0 < E_A$ . For these conditions, the numerical calculations predict a superlinear behavior in the space charge field dependence on  $m$ . This is demonstrated in curve (a) in Fig. 5, corresponding to  $\Lambda = 200 \mu\text{m}$ .

The magnitude of the correction parameter,  $a$ , as determined from a fit of Eqn. (24) to the numerical results, depended upon the crystal parameters and the external conditions, and could be correlated with an enhancement parameter  $R$ , defined as:

$$R = \frac{E_0}{(E_A + E_D)} X \quad (25)$$

where  $X (\approx 1)$  is dependent on the grating period. In Fig. 6 we plot  $a$  vs  $R$ , where we have set  $X = 1$ . Different  $R$  values were obtained by varying the grating period,  $\mu\tau$ , and applied electric field. The magnitude of the correction parameter exhibited an approximate linear dependence on  $R$  over the range of  $R = 0.7$  to 7. It was observed that an improved fit could be obtained by defining  $X$  according to

$$X = 1 + b \frac{\Lambda}{L_E}, \quad (26)$$

where  $b$  is a small number, determined empirically. This reflects

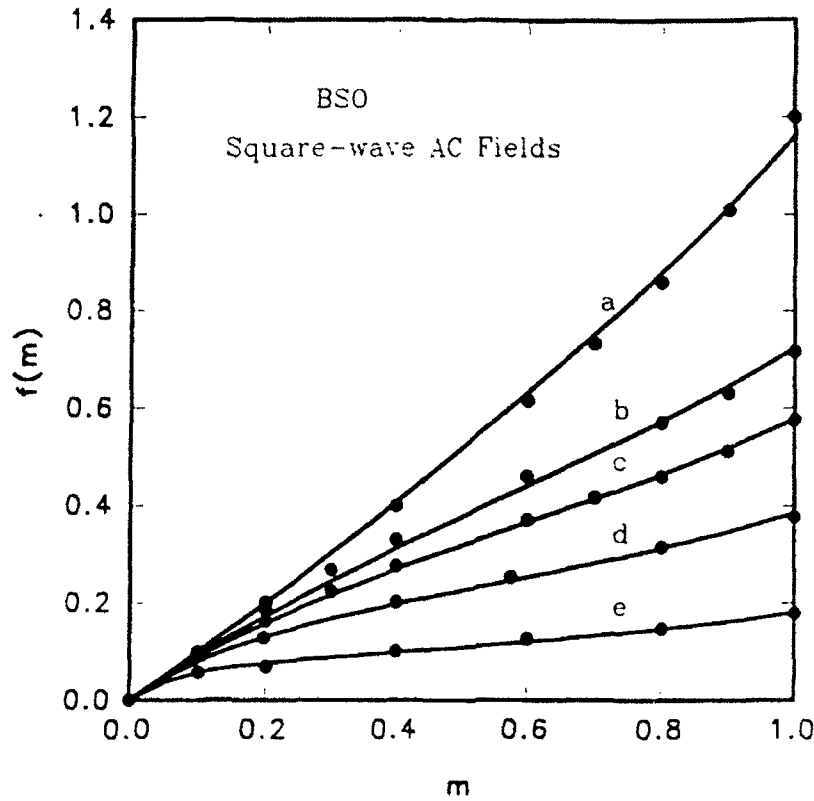


Figure 5. Calculated correction function vs modulation index for applied square-wave ac fields in BSO. (a)  $\mu\tau = 1.9 \times 10^{-7} \text{ cm}^2/\text{V}$ ,  $\Lambda = 200 \text{ } \mu\text{m}$ ,  $E_A = 10 \text{ kV/cm}$ , (b)  $\mu\tau = 6.2 \times 10^{-8} \text{ cm}^2/\text{V}$ ,  $\Lambda = 4 \text{ } \mu\text{m}$ ,  $E_A = 10 \text{ kV/cm}$ , (c)  $\mu\tau = 1.9 \times 10^{-7} \text{ cm}^2/\text{V}$ ,  $\Lambda = 60 \text{ } \mu\text{m}$ ,  $E_A = 10 \text{ kV/cm}$ , (d)  $\mu\tau = 1.9 \times 10^{-7} \text{ cm}^2/\text{V}$ ,  $\Lambda = 30 \text{ } \mu\text{m}$ ,  $E_A = 10 \text{ kV/cm}$ , (e)  $\mu\tau = 6.2 \times 10^{-7} \text{ cm}^2/\text{V}$ ,  $\Lambda = 30 \text{ } \mu\text{m}$ ,  $E_A = 10 \text{ kV/cm}$ . The solid lines are a fit of the numerical results to the equation  $f(m) = 1/a[1 - \exp(-am)] \exp(m)$ . The values of  $a$  determined from the fit were: (a) 2.0, (b) 3.2, (c) 4.7, (d) 7.1, (e) 15.1. The dashed line indicates  $f(m) = m$ .

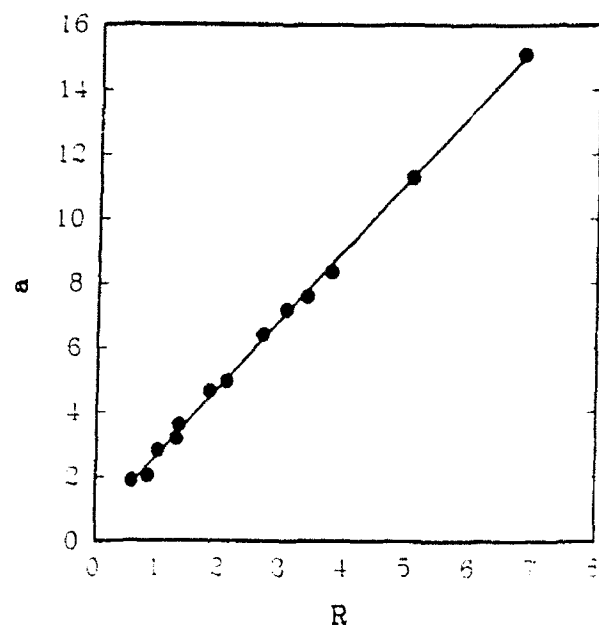


Figure 6. Correction parameter vs enhancement parameter  $R$ , with  $X = 1$ .

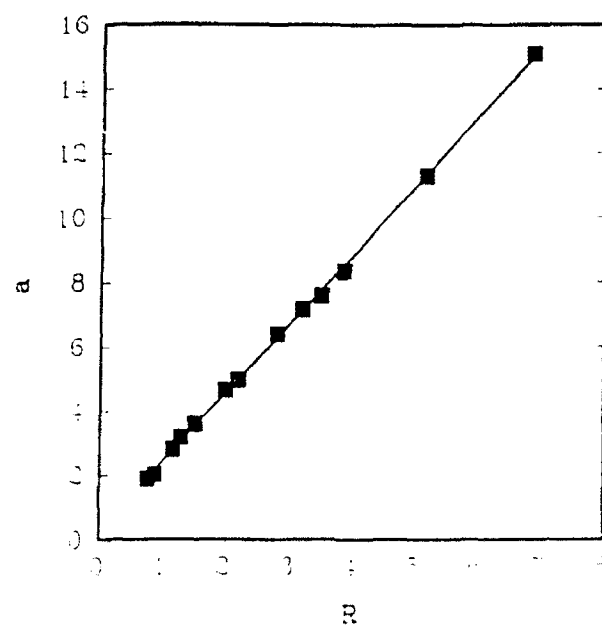


Figure 7. Correction parameter vs enhancement parameter  $R$  defined by equations (25-26), and  $b = 0.03$ .

a reduced efficiency in the space charge field formation for grating periods larger than the drift length. The dependence of the correction parameter  $a$  on the enhancement parameter  $R$ , with  $X$  defined by eqn. (26) and  $b = 0.03$  is shown in Fig. 7. This dependence can be approximated as

$$a = 2.15R + 0.31. \quad (27)$$

Equations (23-27) approximate well the numerical results and can be used to predict and model the photorefractive behavior for other crystal parameters and external conditions.

Further insight into the effects of large modulation on the grating formation can be obtained from examination of the spatial distribution of the space charge field. In Fig. 8 we show the calculated space charge field along one grating period for  $m = 1$  in BTO at  $E_A = 10$  kV/cm. The field distribution could be characterized as a square wave function. The fundamental component of the space charge field at large modulation could be about 20% greater than the applied field, but the contributions from the higher harmonics lowered the peak amplitude of the total space charge field to a value closer to the applied field. The amplitude of the higher harmonic components depended upon the magnitude of the saturation. In general, at  $m = 1$  the second harmonic component was relatively weak,  $< 5\%$  of  $E_1$ , while the third harmonic was about 30% of the fundamental, characteristic of a square-wave profile. Even for crystal parameters and external conditions for which the saturation was not very strong the third harmonic component was still greater than the



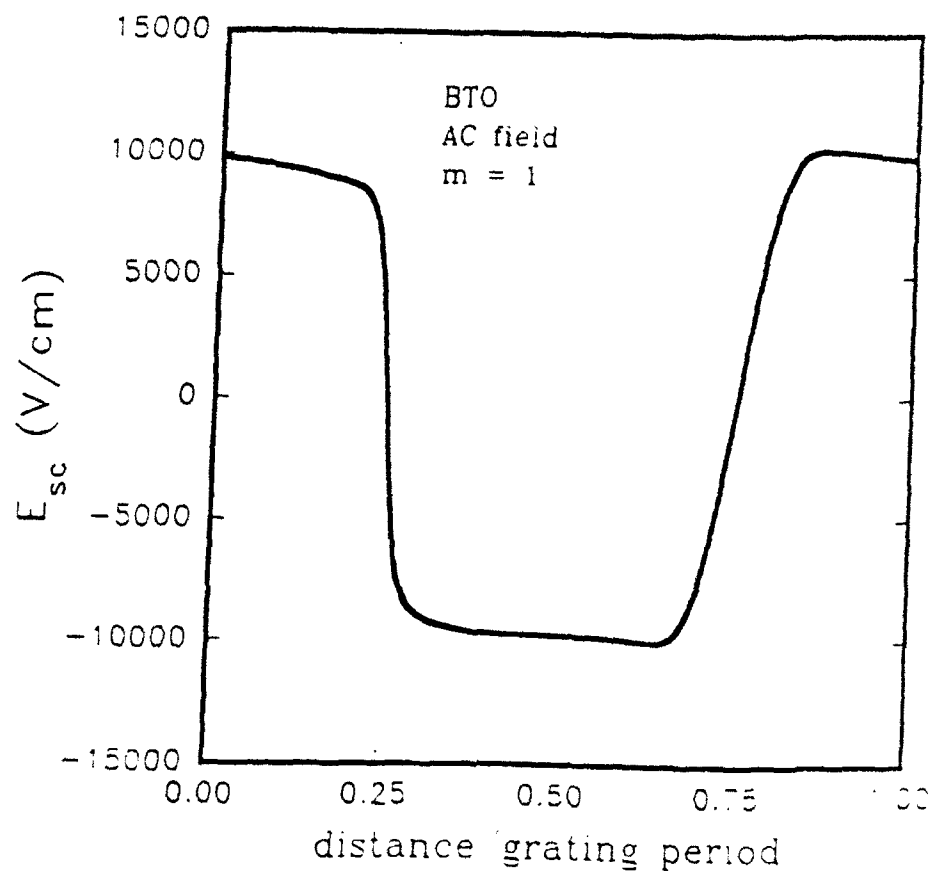


Figure 8. Space charge field distribution along one grating period in BTO for an applied square-wave ac field of 10 kV/cm at modulation index  $m = 1$  and  $R = 3.9$ .

second harmonic at  $m = 1$ .

The temporal behavior of grating formation was also affected at large modulation. This is demonstrated in Fig. 9 where we plot the magnitude of the fundamental component of the space charge field normalized by the modulation index for different values of  $m$  as a function of normalized time,  $t/\tau_g$ . Here  $\tau_g$  is the grating formation time constant determined from the linearized theory. The results shown in Fig. 9 are for BTO with  $E_A = 10$  kV/cm. At small  $m$  the space charge field exhibited the expected exponential growth. At larger modulation the early time response of the space charge field was as expected from the linearized theory, but now also exhibited oscillatory behavior. At much larger modulation this oscillatory behavior was no longer evident, as the space charge field "clamped" at a limiting value which was on the order of the applied electric field.

These characteristics suggest that the fundamental component of the space charge field may be written as

$$E_1(t) = f(m)E_0[1 - \exp(-t/\tau_e)\cos(\omega_e t)] \quad (28)$$

where  $\tau_e$  and  $\omega_e$  are functions of  $m$  and  $R$ . This equation described well the main features of the time dependence but not the fine details of the oscillations. Noting that at very early times  $E_1(t)/m$  is independent of  $m$ , Eq. (28) implies that

$$\tau_e = \frac{f(m)}{m} \tau_g. \quad (29)$$

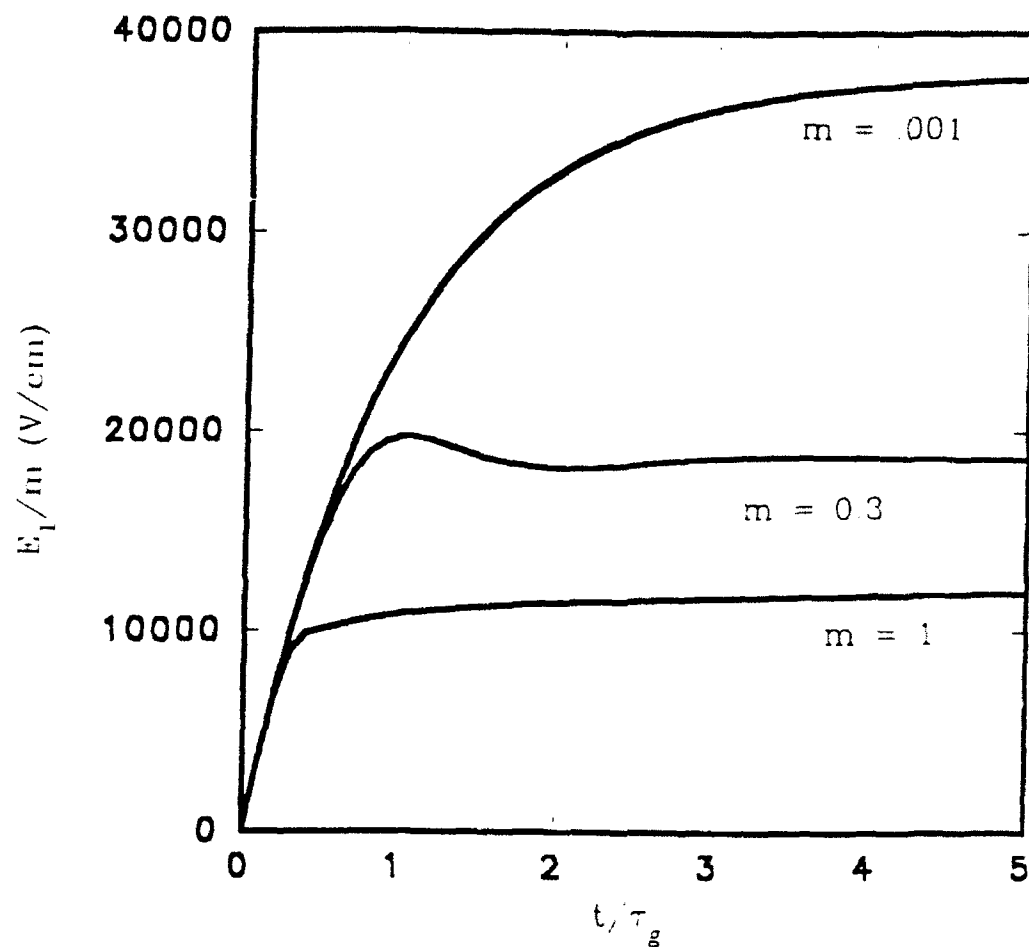


Figure 9. Normalized fundamental component of the space charge field vs normalized time for different values of modulation index in BTO.

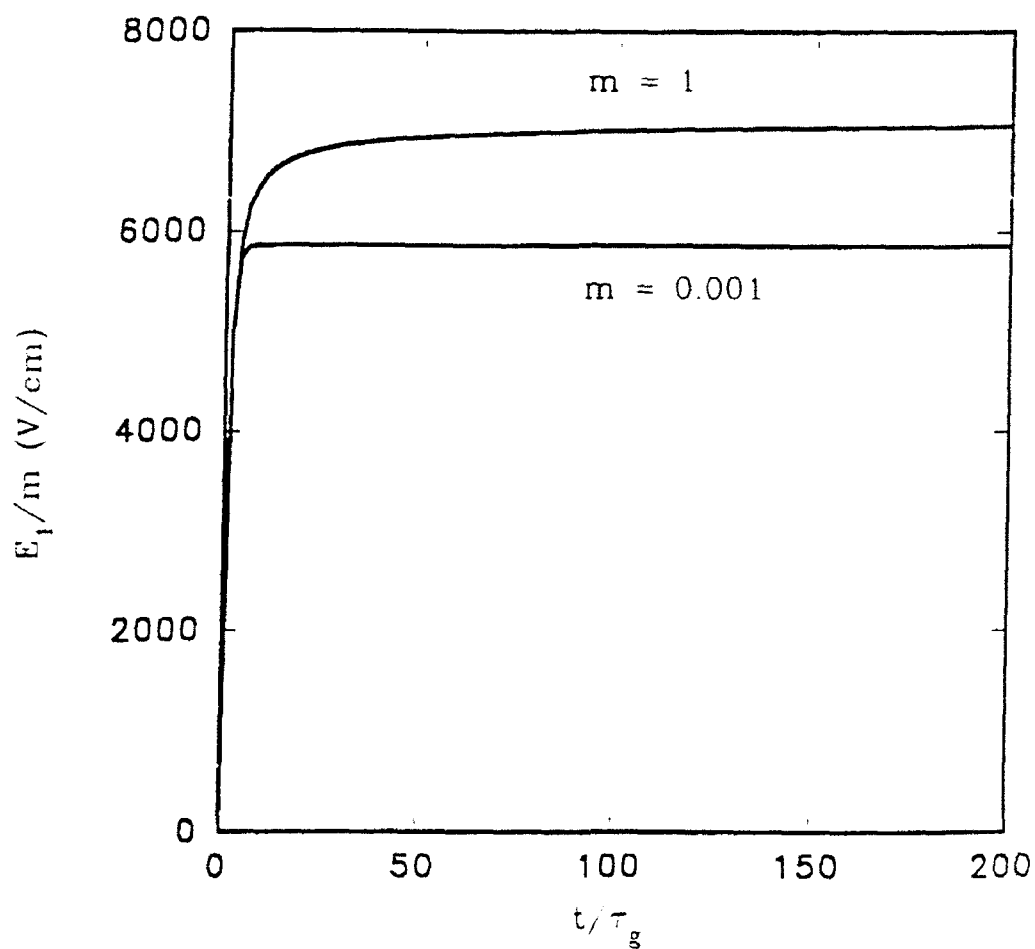


Figure 10. Normalized fundamental component of the space charge field vs normalized time for an applied square-wave ac electric field corresponding to superlinear behavior for  $m = 1$  and  $m = 0.001$ .

This value for the grating time constant did agree well with the calculated time dependence, for  $R > 1$ . The value of  $\omega_e$  depended on  $R$  and  $m$  in a complicated manner. When  $m$  was small,  $\tau_e \approx \tau_g$  and  $\omega_e \ll 1/\tau_e$ . In this limit Eq. (28) agreed with the linearized theory. For  $m > 0.1$ ,  $\omega_e$  was on the order of  $1/\tau_e$ .

At large modulation Eq. (28) no longer provided a good description of the temporal behavior due to the clamping of the space charge field. It was convenient to characterize the time response by a single exponential. For the case shown in Fig. 9 the effective grating formation time constant at  $m = 1$  decreased by a factor of 5 over that at small  $m$ . The change in the effective grating time constant depended on the magnitude of the saturation.

For small  $R$ , corresponding to superlinear grating formations, the effective time constant was greater than  $\tau_g$ . In these cases the grating continued to grow over many time constants, as demonstrated in Fig. 10 where we compare the time dependence of the grating formation for small and large  $m$ .

The effects of large modulation on sinusoidal ac fields were also considered. With sinusoidal ac fields the magnitude of the induced space charge field was much less than that for square wave fields,  $R \approx 0.75$ . Consequently, the large signal effect associated with square wave-ac fields was not present for sinusoidal ac fields. A typical result for the applied sine wave ac field is shown in Fig. 11 for BSO at  $30 \mu\text{m}$  grating period and  $E_A = 10\text{kV/cm}$ . The fundamental component of the space charge field increased superlinearly with modulation index, and could be

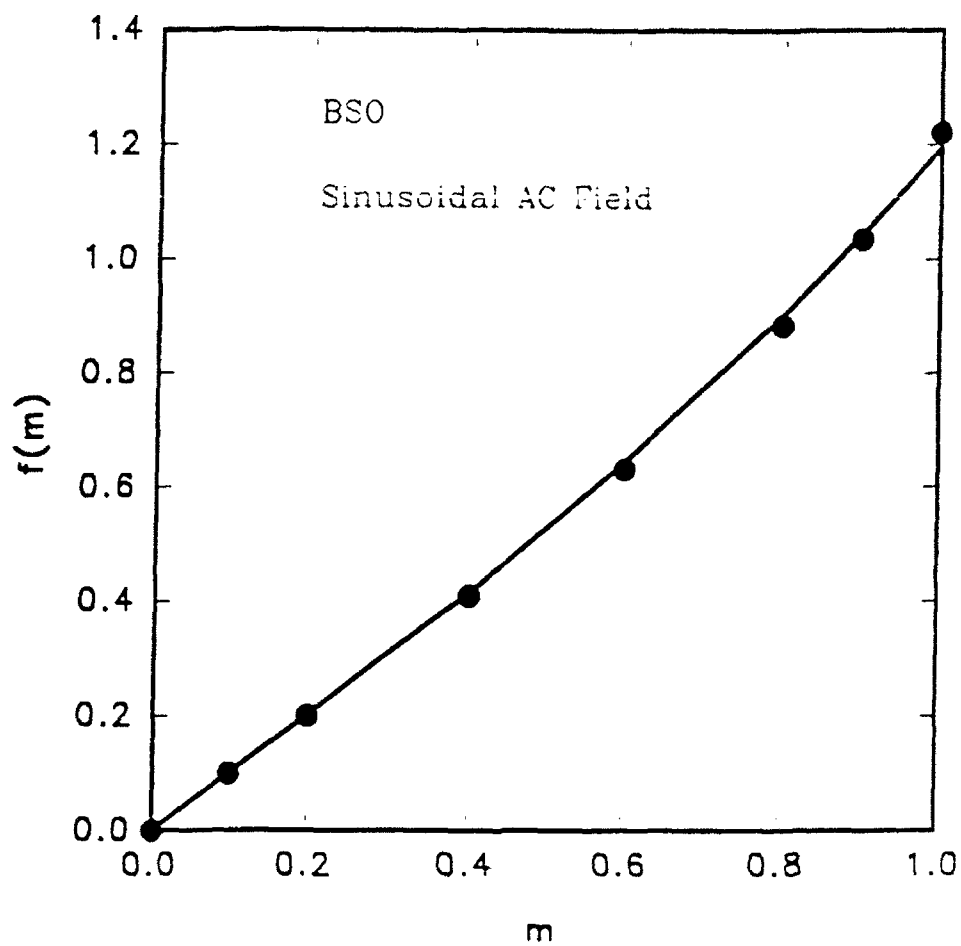


Figure 11. Calculated correction function vs modulation index for an applied sinusoidal ac electric field in BSO.

described by the correction function  $f(m)$  given by eqn. (24). The spatial profile along one grating period for  $m = 1$  is shown in Fig. 12. As this profile indicates, the peak amplitude of the space charge field was able to become nearly as large as that of the applied field. At large  $m$  the grating formation exhibited a very long, slow growth, similar to that of the superlinear square-wave behavior shown in Fig. 10.

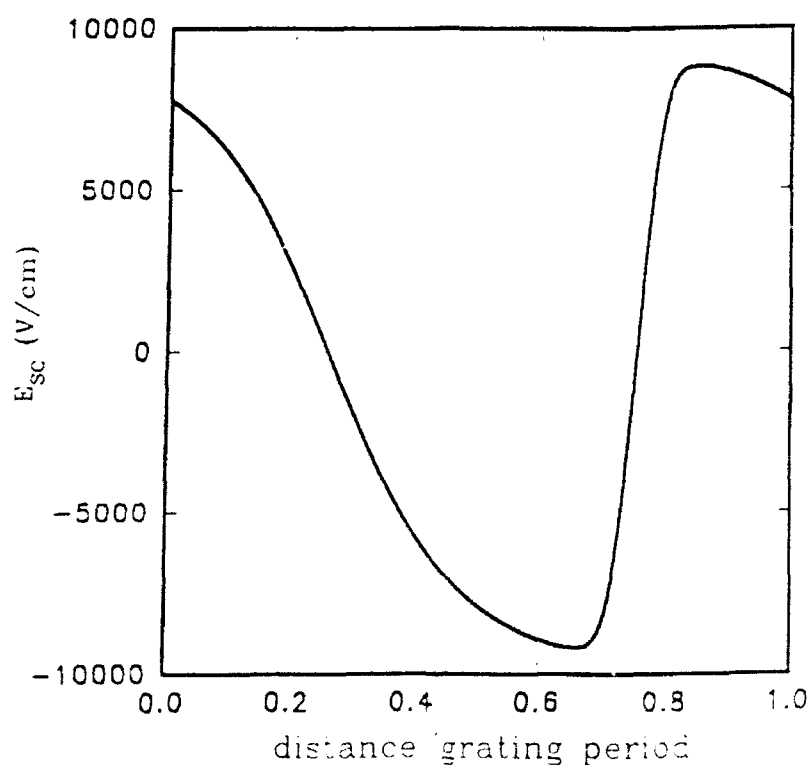


Figure 12. Space charge field distribution along one grating period in BSO for an sinusoidal ac field of 10 kV/cm at modulation index of 1.

### 3.1.3 Discussion

As the numerical solutions show, the space charge field is limited in magnitude to approximately the amplitude of the applied electric field. The existence of this upper limit to the space charge field was not unexpected, and is similar to that found by Swinburne et al.[14] and suggested by Stepanov and Sochava[13]. The large enhancements with the nonstationary techniques stem from drift assisted charge redistribution. When the space charge field becomes comparable in magnitude to that of the applied electric field charge transport becomes inhibited, limiting the growth of the space charge field. We note that although the higher harmonics need to be considered, the large signal effects are not due to competition from the higher harmonics, as is frequently suggested. For square-wave ac fields the presence of the higher harmonics apparently enhance the space charge field by allowing  $E_1$  to become somewhat larger than  $E_A$ . Even in those cases where the space charge field increased superlinearly, the higher harmonic components were significant.

The results of the numerical calculations, which reflect a range of crystal parameters and conditions, have been expressed in a simple analytical form through Eqs. (23-27). These analytical expressions are quite general and are appropriate for most applications of square wave ac fields in BSO and BTO. One difficulty with the numerical solutions is the establishment of limits for which these equations may be applied. We can identify some limits based on physical arguments. Equations (23-



17) should not be expected to apply when the space charge field is trap limited or when charge redistribution has a significant diffusion contribution. These conditions will exist at small grating periods and low electric field strengths, or small  $N_e$ . We have carried out some calculations to test these expectations. In the former case, the space charge field increased approximately linearly with  $m$  for  $E_0 \approx E_q$ ,  $E_A > E_q$ . In the latter case, the analytical expressions under-estimated the space charge field at large  $m$  for  $E_A < 2E_D$ .

The results presented above refer to the microscopic space charge field. When comparing with experimental data, beam coupling effects must be taken into consideration as the modulation index will vary in the  $z$  direction. Utilizing the correction function  $f(m)$  the coupled wave differential equations can be written as:[7]

$$\frac{dI_R}{dz} = -\Gamma_S \frac{f(m)}{m} \frac{I_R I_S}{I_R + I_S} - \alpha I_R \quad (30)$$

and

$$\frac{dI_S}{dz} = \Gamma_S \frac{f(m)}{m} \frac{I_R I_S}{I_R + I_S} - \alpha I_S \quad (31)$$

where

$$\Gamma_S = \frac{2\pi r_{eff} n^3 E_0}{\lambda \cos(\theta)} \quad (32)$$

is the gain coefficient,  $\alpha$  is the absorption coefficient,  $I_R$  is the reference beam,  $I_S$  is the signal beam,  $r_{eff}$  is the effective electro-optic coefficient, and  $n$  is the refractive index.

As an application of the analytical equations and a demonstration of the "large signal effect" we calculated the two-beam coupling gain coefficient for different input beam ratios and crystal thickness vs grating period. These results are shown in Fig. 13. The gain curves were calculated for crystal parameters of  $\mu r = 1.9 \times 10^{-7} \text{ cm}^2/\text{V}$ ,  $\epsilon = 56$ ,  $N_e = 10^{16} \text{ cm}^{-3}$ , and  $r_{eff} = 5 \text{ pm/V}$ , with  $E_A = 5 \text{ kV/cm}$ . In Fig. 13, we plot the gain coefficient as determined by the linearized theory of Stepanov and Petrov[8], labeled as curve (a). Curves (b-d) correspond to the gain coefficient for beam ratios of  $10^6$  and  $10^2$  ( $m = 0.002$  and  $0.2$ ) and crystal thicknesses of  $1 \text{ mm}$  and  $10 \text{ mm}$ . The gain was calculated by numerical solving the coupled wave equations (30-32) with  $f(m)$  determined according to equations (24-27). The effective gain coefficient was then determined from the calculated gain according to [7,19]

$$\Gamma = \frac{1}{d} \ln[\gamma_0 \beta / (\beta + 1 - \gamma_0)] \quad (33)$$

where  $\gamma_0$  is the numerically calculated gain and  $d$  is the interaction length. Eq. (33) accounts for beam coupling effects and gives  $\Gamma = \Gamma_S$ , provided that  $f(m) = m$ . Any departure of the gain curves from that of curve (a) is an indication of the nonlinearity in the space charge field dependence on  $m$ . For curve (b), corresponding to  $\beta = 10^6$  and  $d = 1 \text{ mm}$ , the linearized

theory was a good approximation. However, for curves (c-d) the nonlinearities resulted in a low effective gain coefficient and a flattened spatial response, as compared to the linearized theory. Not only were the nonlinear effects substantial for  $\beta = 10^2$ , but as curve (c) shows, also for  $\beta = 10^6$  with a 10 mm thick crystal. It is important point to note here that with square wave ac fields the linear-in-modulation approximation is generally not valid, even for relatively large beam ratios.

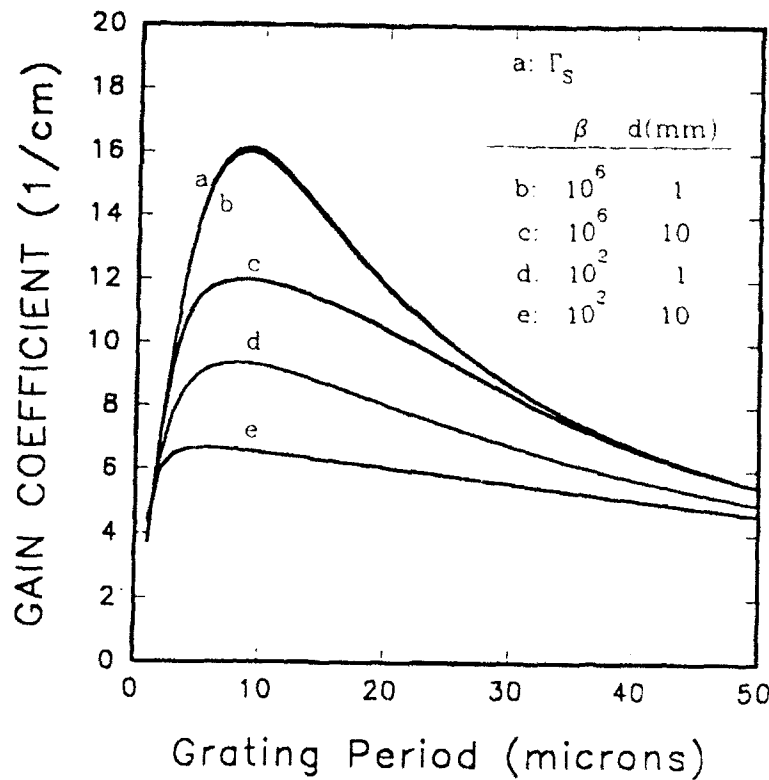


Figure 13. Calculated effective gain coefficient vs grating period in BSO for different input beam ratios and crystal thicknesses. (a)  $\Gamma = \Gamma_s$ , (b)  $\beta = 10^6$ ,  $d = 1\text{mm}$ , (c)  $\beta = 10^6$ ,  $d = 10\text{mm}$ , (d)  $\beta = 10^2$ ,  $d = 1\text{mm}$ , (e)  $\beta = 10^2$ ,  $d = 10\text{mm}$ .

### 3.1.4 Experimental Results

The photorefractive response with ac electric fields was measured experimentally in BTO. Experiments were conducted on a 1.37 mm x 3.56 mm x 2.74 mm (001) grown at Hughes Research Laboratories. The two large faces were antireflection coated to eliminate spurious gratings. The short sample length of 1.37 mm was chosen to reduce the effects of optical activity and pump depletion. A linearly polarized helium-neon laser was used for the two-wave mixing experiments. The two-wave mixing gain was measured as a function of beam ratio for different applied fields and grating periods. These results are shown in Figures 14-15. The experimental data reflect the intensity gain. The bold curves in each plot are the theoretical predictions, calculated for the measured crystal parameters of  $N_{\text{eff}} = 3 \times 10^{16} \text{ cm}^{-3}$ ,  $\mu\tau = 6.8 \times 10^{-8} \text{ cm}^2/\text{V}$ , and  $r_{\text{eff}} = 5.4 \text{ pm/V}$ . Equations 30 and 31 were solved numerically to calculate the theoretical gain using the correction function derived above. There were no free parameters.

Figure 16 shows the time response of the two-beam coupling process for two different beam ratios. The effective response time was decreased by a factor of 19 at large modulation.

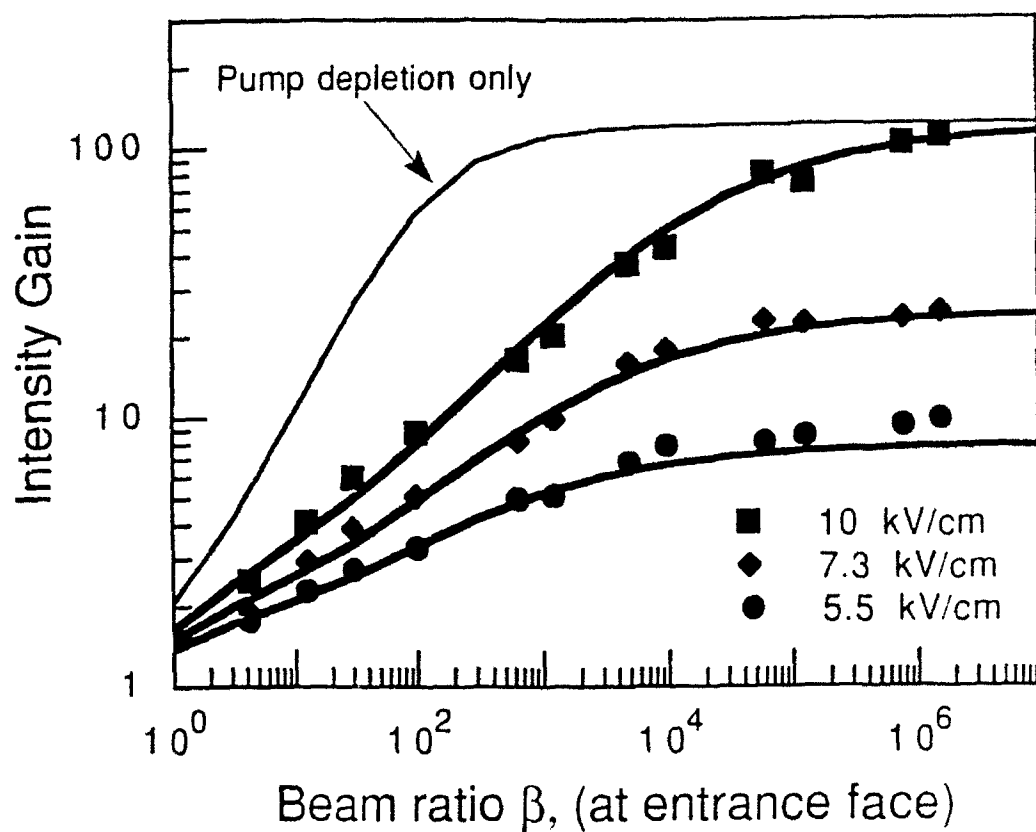


Figure 14. Two-wave mixing gain versus input beam ratio in BTO. Bold curves are results of numerical model. The thin curve is the standard linearized theory for the 10-kV/cm case.

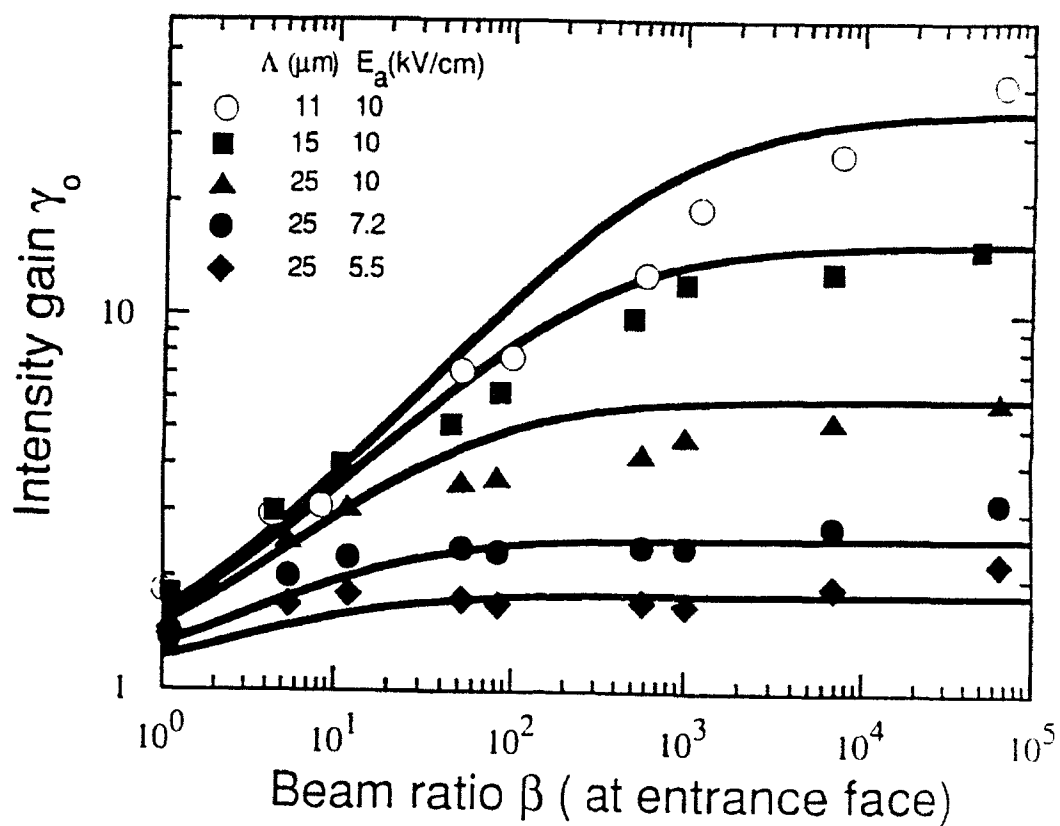


Figure 15. Two-wave mixing gain versus input beam ratio for several grating spacings and applied fields. Curves are from the analytical expressions of the numerical model.

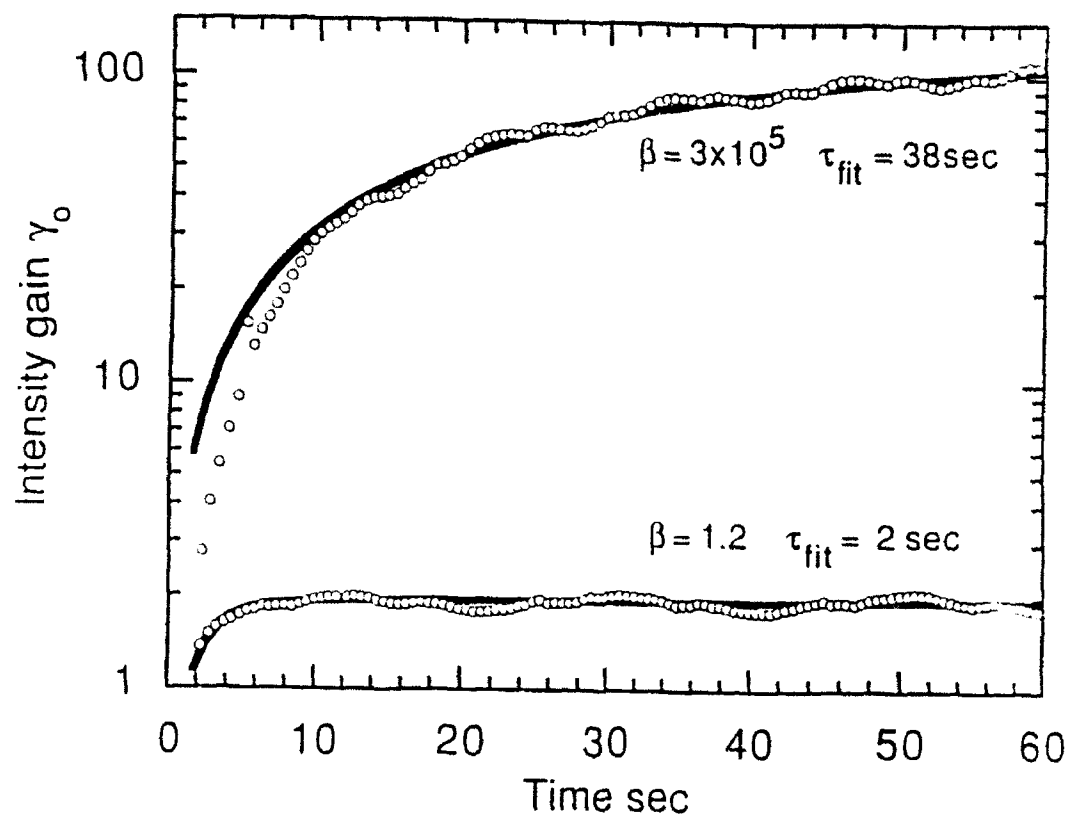


Figure 16. Time response of the two-wave mixing process for two different beam ratios. Grating period is  $6.1 \mu\text{m}$ , total intensity is  $100 \text{ mW/cm}^2$ .

As these results show, the numerical model accurately predicted the steady-state photorefractive response for ac fields, both square-wave and sine-wave. In comparing the temporal characteristics predicted above and shown in Fig. 9 with experimental results we note that the two-beam coupling time constant is different than the grating formation time constant, and depends upon the gain coefficient and interaction length. Using the following relation

$$\gamma(t) = \exp[df(m)\Gamma_S(1-\exp(-t/\tau_e))]. \quad (34)$$

with  $\Gamma = 35\text{cm}^{-1}$  and  $d = 0.137\text{ cm}$ , the numerical results predict a decrease in the two-beam coupling gain time constant by a factor of approximately 10 at  $m = 1$ , when compared to small  $m$ . Although quantitative comparison between the numerical calculations and the experimental results is difficult because of time-dependent changes in the modulation index, this result compares well with the experimental factor of 19.

### 3.1.5 AC Field Frequency Dependence

The influence of the ac field frequency on the photorefractive characteristics was also examined. Previously, the small modulation solutions had been time averaged. No attention been given to the temporal variations in the phase and magnitude of the grating. These are important parameters in signal processing. The numerical analysis was therefore extended to investigate the ac field frequency dependence. In this



analysis a parameter  $Q$  was defined as the ratio of the grating formation time constant to the period of the ac field:

$$Q = \tau_g / T_{AC}. \quad (36)$$

Results of the analysis are shown in Figures 17 - 21. The parameter values were  $\mu\tau = 1.9 \times 10^{-7} \text{ cm}^2/\text{V}$ ,  $N_{\text{eff}} = 10^{16} \text{ cm}^{-3}$ ,  $\epsilon = 56$ , and a grating period of  $20 \text{ }\mu\text{m}$ , values appropriate for BSO. The plots in Figures 17 and 18 show the time averaged amplitude of the fundamental component of the space charge field as a function of frequency and  $Q$  for different grating formation time constants. Figures 19 and 20 show the temporal response over one time period of the applied ac field for  $Q$  values of 3 and 10, calculated for a 10 ms grating time constant. As these results show, the space-charge field amplitude exhibited a modulation at two times the ac field frequency, and the spatial phase of the fundamental component exhibited a oscillation about a  $90^\circ$  phase shift with a frequency of the applied ac field. The magnitude of the oscillation depended upon the  $Q$  factor, decreasing with increasing  $Q$ , as shown in Figure 21. This analysis indicates that  $Q > 50$  is required for phase stability  $\leq 1^\circ$ . Amplitude stability of much less than 1% is easily obtained. However, it should be noted that if high intensities are used to decrease the response time, then damped high frequency oscillations may be present due to free carriers, whose contribution to the space charge grating increases with increasing intensity.

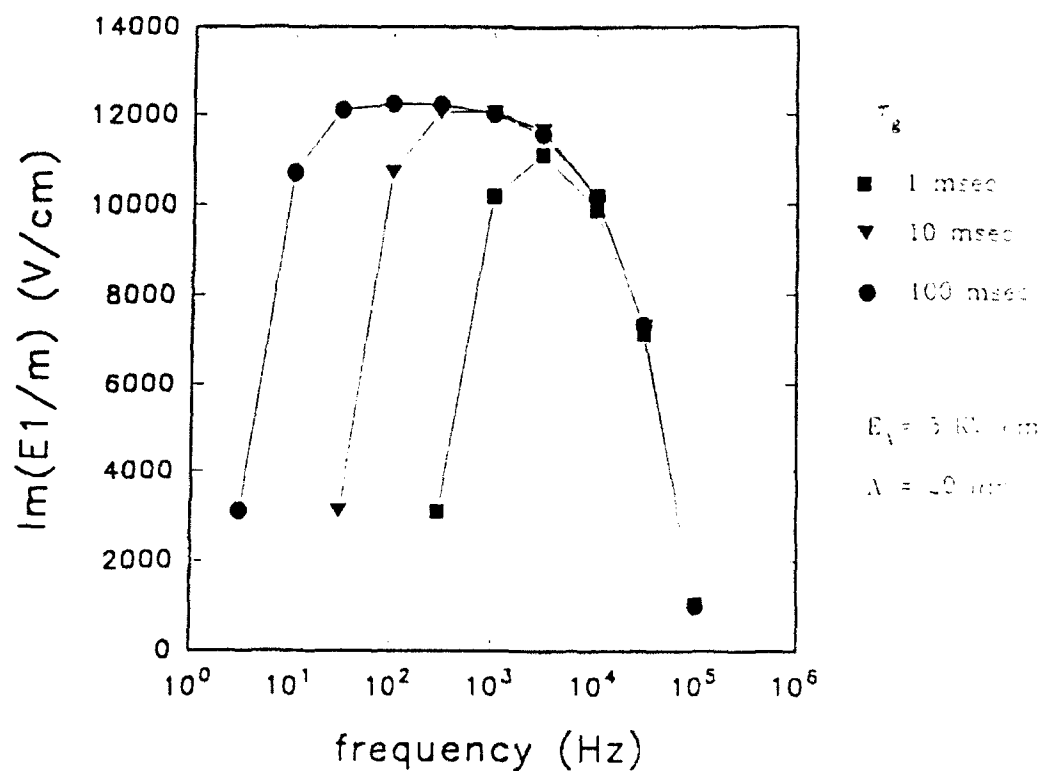


Figure 17. Space charge field magnitude versus frequency for different grating formation time constants.

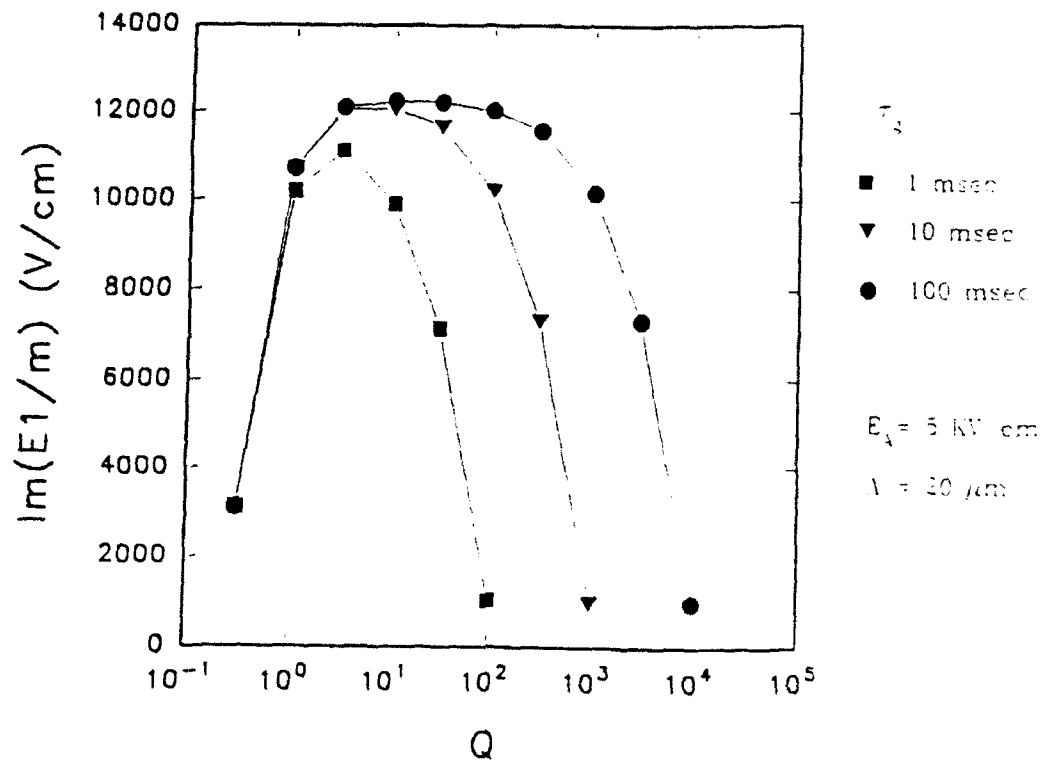


Figure 18. Space charge field magnitude versus  $Q$  for different grating formation time constants.

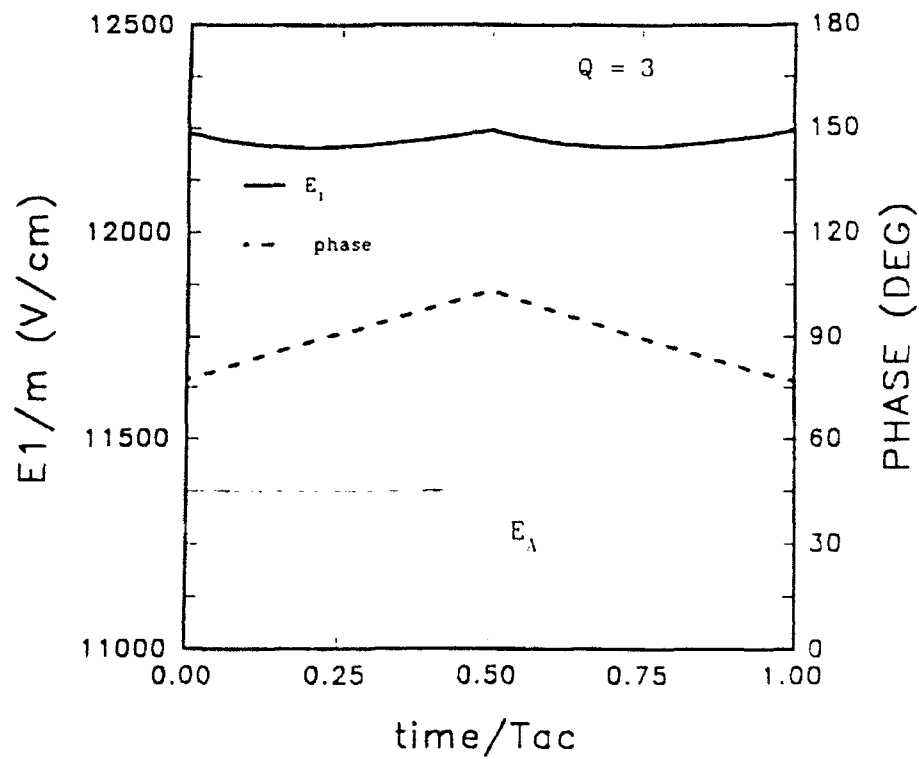


Figure 19. Temporal response over one time period of the ac field for  $Q = 3$ .

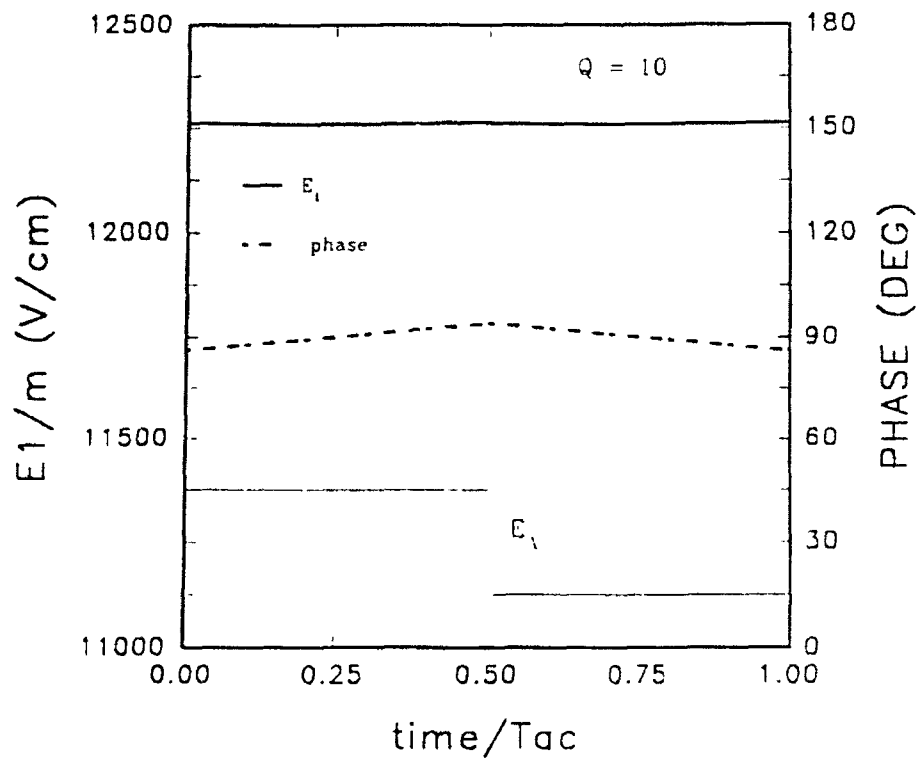


Figure 20. Temporal response over one time period of the ac field for  $Q = 10$ .

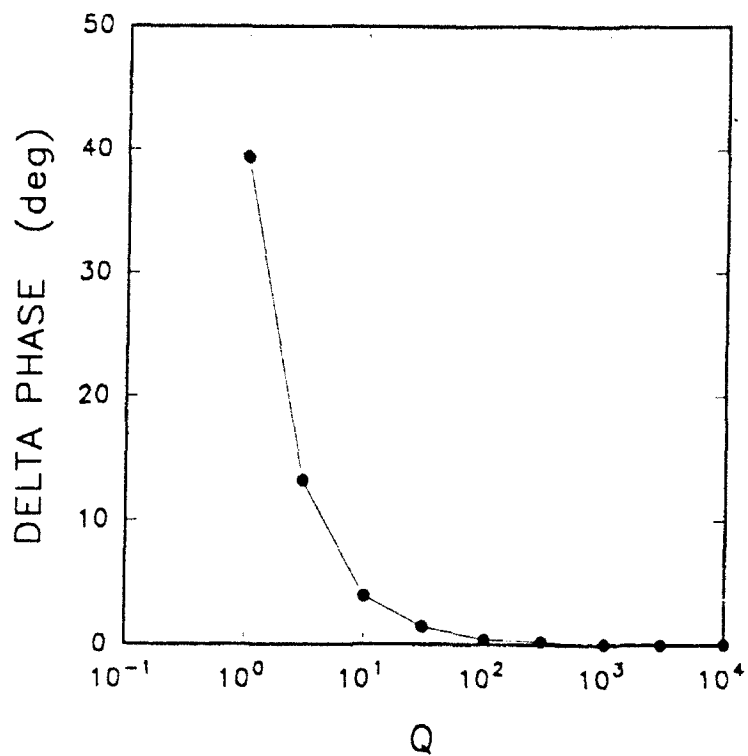


Figure 21. Phase modulation versus Q factor for square-wave ac field.

### 3.2 Moving Gratings

The moving grating technique was considered also. The moving grating technique involves the application of a dc field in combination with a frequency detuning of one of the laser beams.[7-12] This technique can significantly increase the magnitude of the space charge field over that which would result from the application of a dc field alone and maximize the component of the index grating at 90°. The enhancements are similar to the ac field technique.

In this section the effects of large modulation under the nonstationary recording conditions of moving interference fringes and an applied electric field are studied in more detail. The finite difference method was used to model the photorefractive grating formations. It is shown that the saturation characteristics can be predicted from crystal parameters over a large range of recording conditions. The numerical results are generalized to other crystal parameters in terms of analytical equations that approximate the numerical solutions.

#### 3.2.1 Small Modulation Theory

In the small modulation index approximation the fundamental component of the space charge field is given by[9]

$$E_1 = \text{im}(-E_A + iE_D)/D_1 \quad (37)$$

where

$$D_1 = -E_A/E_Q + b(1 + E_D/E_M) + i(1 + E_D/E_Q + bE_A/E_M)$$

$$E_D = Kk_B T/q, \quad E_Q = qN_e/(\epsilon\epsilon_0 K), \quad E_M = \gamma_R N_e/\mu K, \quad (38)$$

$$b = Kv\tau_{die}$$

and  $v$  is the fringe velocity. The normalized velocity that maximizes  $\text{Im}(E_{SC})$  is given by

$$b_{opt} = A[1 \pm (1-G/A^2H)^{1/2}] \quad (39)$$

where

$$\begin{aligned} A &= E_A/E_Q + E_D/E_A(1 + E_D/E_Q), \quad B = E_M/E_D, \\ c &= E_M/E_D(1 + E_D/E_Q), \quad f = (E_D + E_M)/E_A, \\ H &= 1 + f^2, \text{ and } G = 2AfB - 2Ac - c^2 - B^2. \end{aligned} \quad (40)$$

At the optimum velocity the imaginary part of the space charge field is given by[7]:

$$\text{Im}(E_{SC}) = mE_0 \quad (41)$$

where

$$E_0 = m \frac{E_M^2}{E_A} \frac{A - b}{(b+c)^2 + (B - bf)^2} \quad (42)$$

### 3.2.2 Numerical Results

In order to determine the characteristics of the space-charge field under conditions of applied ac fields the grating formation



was modeled with the finite difference scheme described in section 3.1. As the numerical method used here was very computer intensive it was practical to calculate grating formations only for a limited, but representative set of parameters. In Figure 22 the calculated amplitude, imaginary component, and phase of the fundamental component of the space charge field are plotted as a function of normalized velocity  $Q = v/v_{opt}$ , at a modulation index of  $m = 0.002$  corresponding to a beam ratio of  $\beta = 10^6$ . The solid lines are the linearized theory given by equation (37). The parameters used for these calculations were  $E_A = 5\text{ kV/cm}$ ,  $N_e = 1 \times 10^{16} \text{ cm}^{-3}$ ,  $\mu\tau = 1.25 \times 10^{-7} \text{ cm}^2/\text{V}$ , and  $\epsilon = 56$ . At small  $m$  the numerical results were in good agreement with the linearized theory. In Figures 23-24 the calculated space-charge field characteristics are shown for other values of modulation index. At large modulation the space charge field exhibits a complicated dependence on velocity. These velocity dependent characteristics are similar to those obtained by Au and Solymar[16].

The imaginary component of the space charge field is an important aspect of the photorefractive response as it affects two beam coupling. As Figures 22-24 indicate, there is no one definite value of fringe velocity that maximizes  $\text{Im}(E_1)$  for all values of  $m$ . It is useful never-the-less to define the optimum normalized velocity  $Q_{opt}(m)$ , as that velocity which optimizes the imaginary part of the fundamental component of the space charge field and is a continuous function of  $m$ . In some cases of very large modulation, such as that shown in Figure 24, this

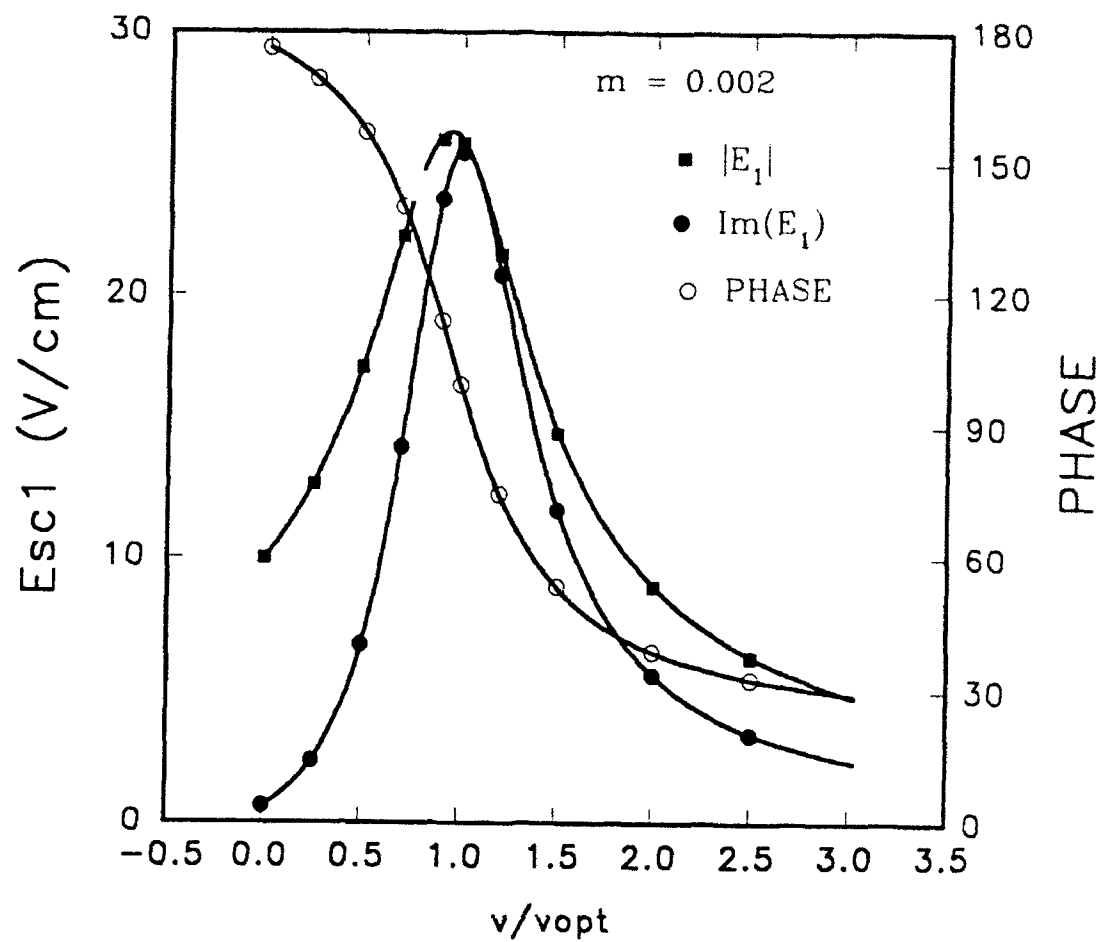


Figure 22. Space-charge field characteristics for moving gratings versus normalized velocity for small modulation. The solid lines are from small modulation theory. Symbols are numerical calculations.

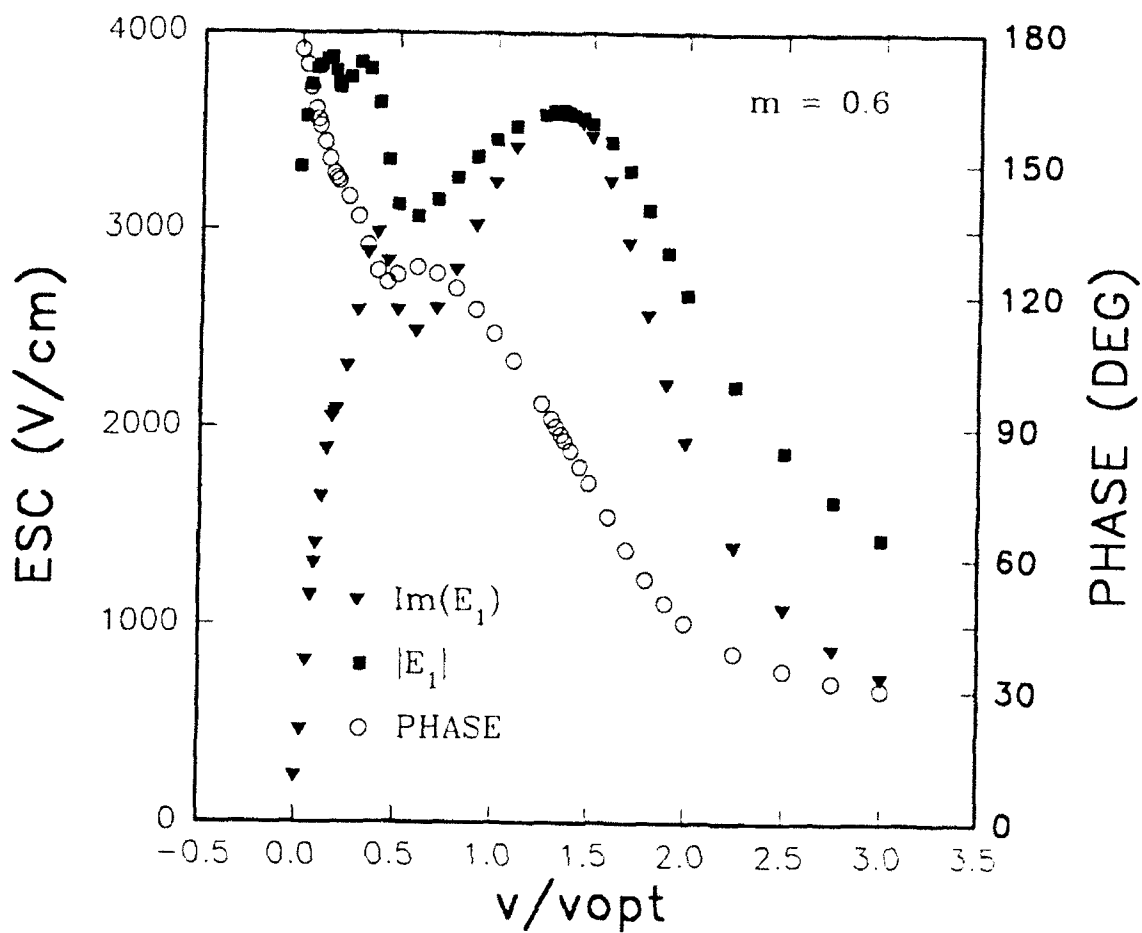


Figure 23. Space-charge field characteristics versus normalized velocity for  $m = 0.6$ . Lines are for visual aid.

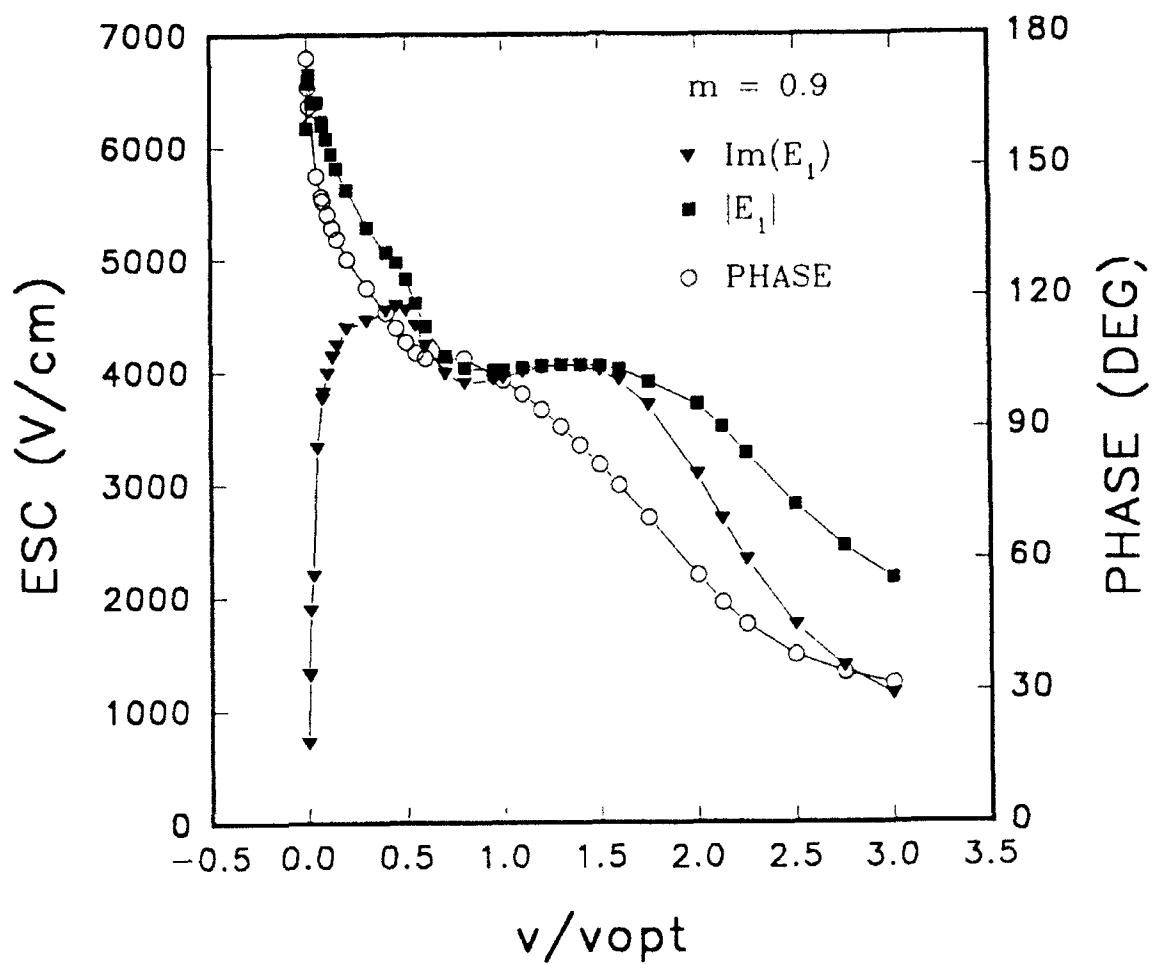


Figure 24. Space-charge field characteristics versus normalized velocity for  $m = 0.9$ . Lines are for visual aid.

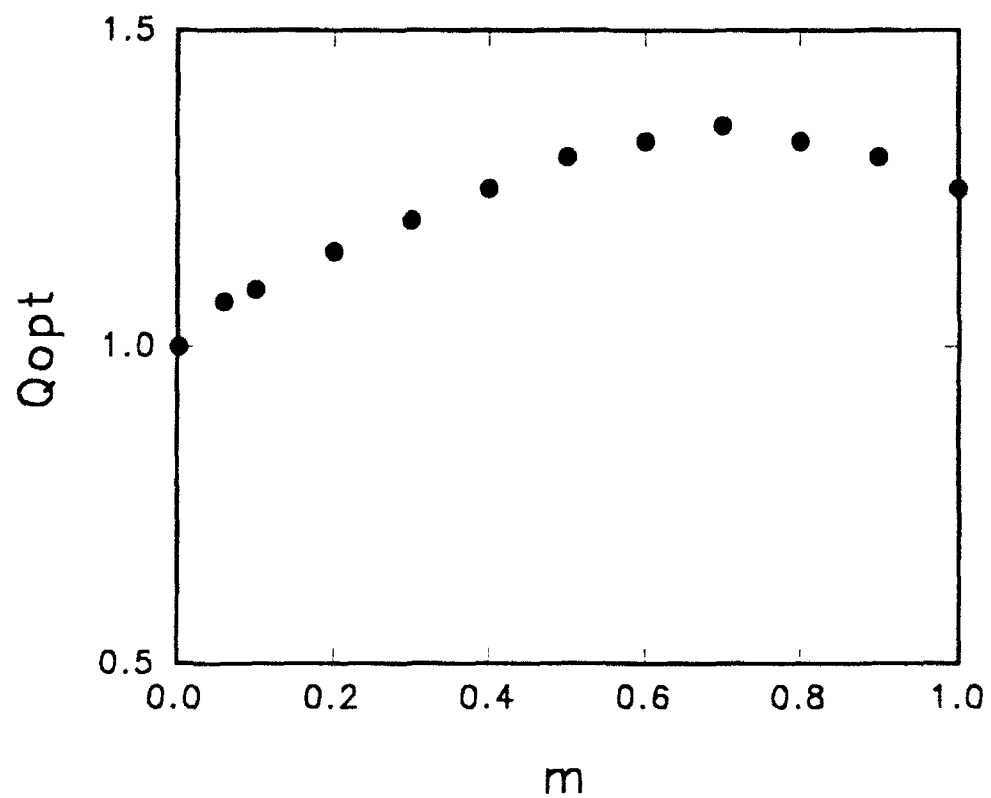


Figure 25. Optimum normalized velocity versus modulation index.

definition of  $Q_{opt}$  does not result in the largest value of  $\text{Im}(E_1)$ . The dependence of  $Q_{opt}$  on  $m$  for the crystal parameters used for Figs. 22-24 is shown in Figure 25. Similar curves were obtained for other crystal parameters. In general,  $Q_{opt}$  is greater than 1, increases with  $m$  until  $m \approx 0.6$ , and then decreases as  $m$  increases towards 1. The phase shift at  $Q_{opt}$  is usually close to  $90^\circ$ .

The dependence of  $\text{Im}(E_1)$  at  $Q_{opt}$  on beam ratio is shown in Figure 26. Here the space charge field is normalized with respect to the applied electric field. Figure 26 demonstrates the large signal effect in which the gain decreases significantly at large  $m$ . According to the linearized theory,  $E_1/m$  should be constant, independent of the beam ratio. The magnitude of the calculated space charge field fell off from the large beam ratio value and declined to a magnitude slightly less than the applied field at  $\beta = 1$ .

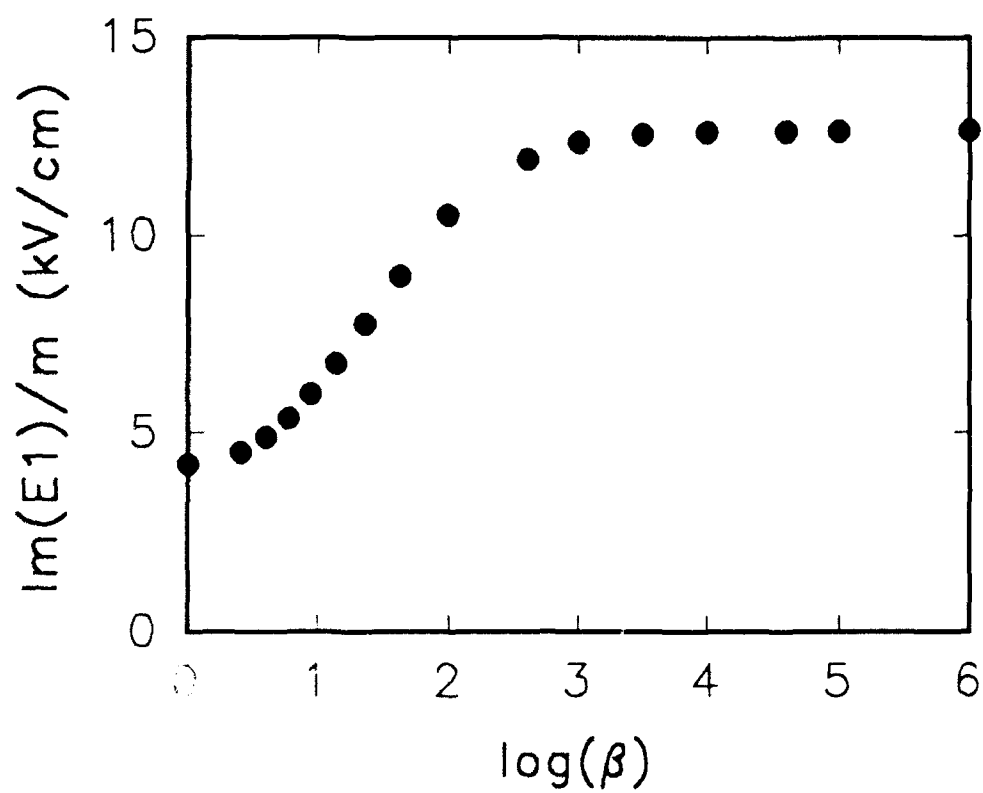


Figure 26. Optimum imaginary part of the fundamental component of the space-charge field versus beam ratio.

These results are again plotted in Figure 27, but as  $f(m)$  vs  $m$ . Here  $f(m)$  is the correction function defined by equation (23). The numerical results show that the value of  $\text{Im}(E_1)_{\text{opt}}$  increased sublinearly with  $m$ , similar to the ac field case.

It is useful to examine the functional form of  $f(m)$ . We consider the equation:

$$f(m) = 1/a[1 - \exp(-am)] \quad (44)$$

determined phenomenologically by Refregier et al.[7] The solid line in Figure 27 is a fit of Eq. (43) to the calculated  $f(m)$ . Similar comparisons were made for other calculations which reflected a range of crystal parameters and recording conditions achieved by varying the values of  $\mu r$ ,  $E_A$ , and grating period. Some of these results are shown in Figure 28. As Figures 27 and 28 show, the correction function  $f(m)$  given by equation (44) provided a fair description of the numerical results over a wide range of saturation characteristics.

A feature of this correction function is that each of the curves in Figures 27 and 28 are characterized by a single correction parameter,  $a$ . The departure of  $f(m)$  from linearity increases with increasing  $a$ . The magnitude of  $a$ , as determined from a fit of eqn. (44) to the numerical results, depended upon the crystal parameters and the external conditions, and could be correlated the enhancement parameter  $R$ , defined in equation (25) with  $X = 1$ .



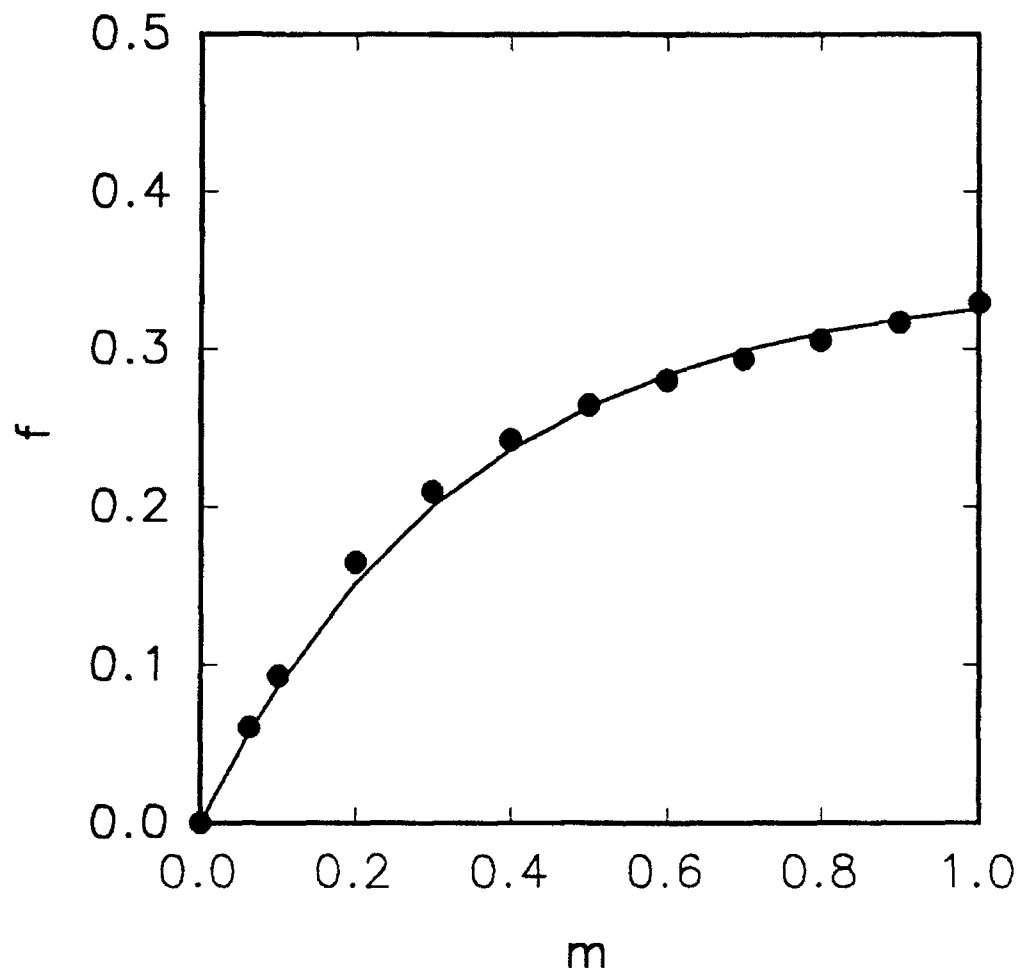


Figure 27. Calculated correction function versus modulation index. The solid line is a fit of equation 44 to the numerical calculations.

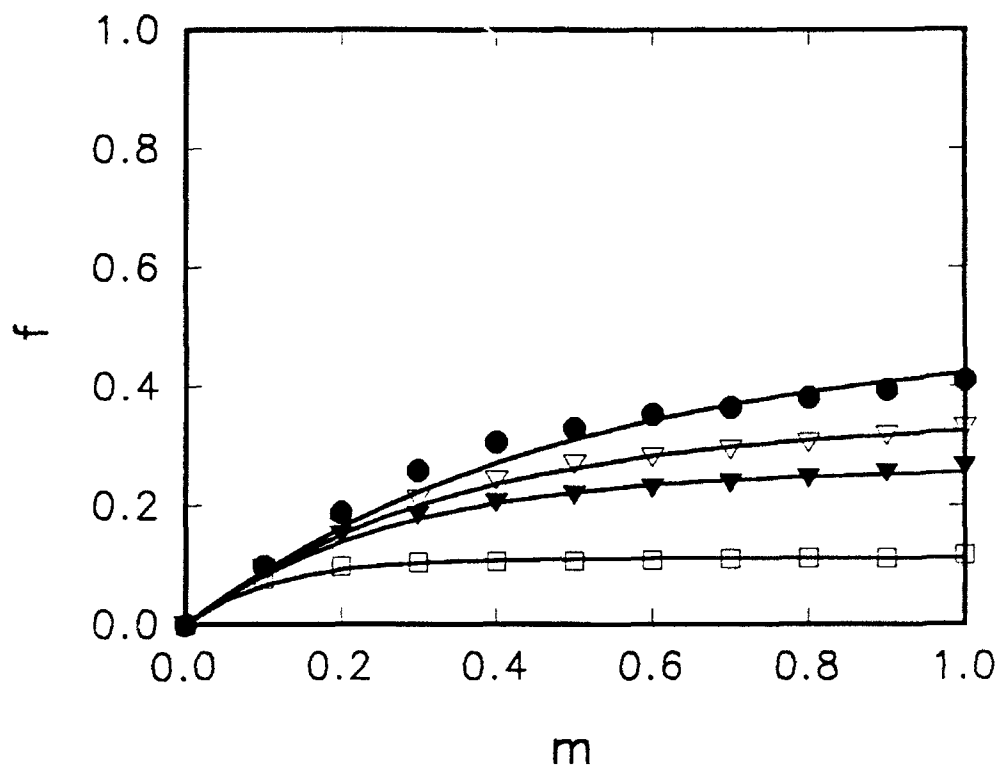


Figure 28. Calculated correction function versus modulation index for different crystal parameters and external conditions. The solid lines are fits of equation 44 to the numerical results.

The magnitude of the correction parameter exhibited an approximate linear dependence on  $R$  over the range of  $R = 1$  to 15, as shown in Figure 29. This dependence can be approximated as

$$a_f = 1.43R - 0.85. \quad (45)$$

Equations (43) -(45) approximate well the numerical results and can be used to predict and to model the photorefractive behavior for other crystal parameters and external conditions.

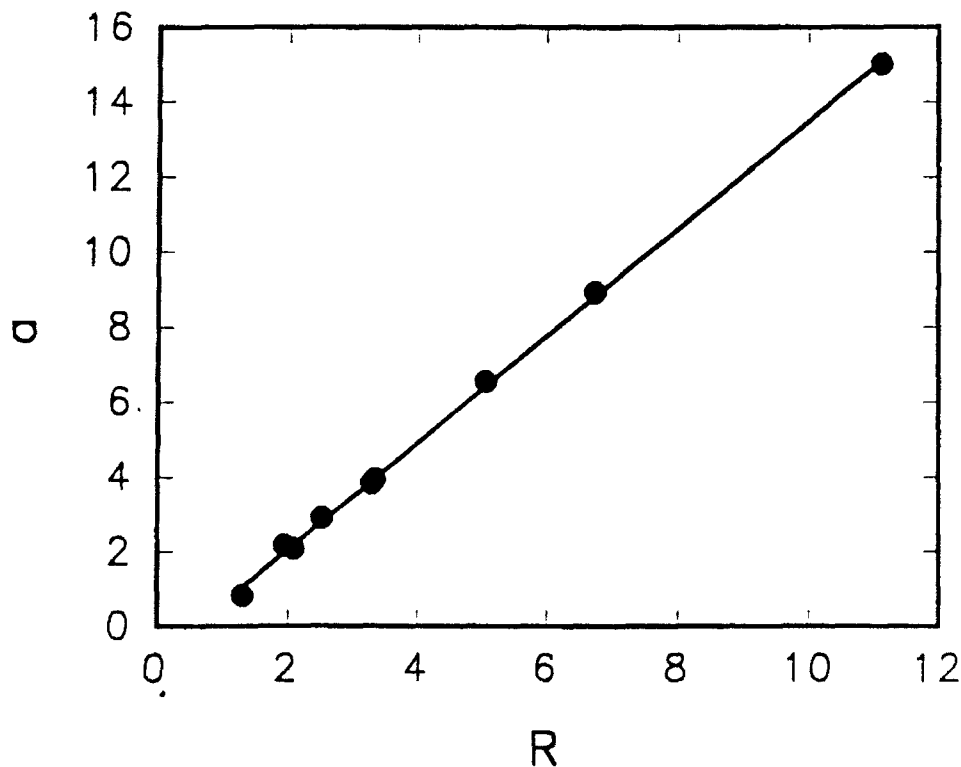


Figure 29. Correction parameter versus enhancement parameter for moving gratings.

#### 4. PHOTOREFRACTIVE CHARACTERIZATION

In this section we report on additional experiments, designed to measure performance characteristics of photorefractive crystals, relevant to the acousto-optic adaptive signal processing application. Experiments were conducted on BSO and BaTiO<sub>3</sub>.

##### 4.1 BSO

A number of BSO crystals were examined, many of which had been supplied by Crystal Technology. In all of these experiments electric fields (1-8 KV/cm) were applied to the crystal. It was observed that in all of the Crystal Technology BSO crystals, a semi-permanent grating was formed which persisted for a few hours even under the illumination of an uniform erase beam. The strength of this fixed grating was similar in magnitude to the dynamic grating which was also formed. A similar effect had been reported previously by Herriau and Huignard.[20] The presence of this persistent grating rendered the Crystal Technology BSO crystals unsuitable for signal processing applications. A BSO crystal obtained from Global Technology, and BSO crystals grown at Rome Laboratory were examined. No persistent grating effects were detected in these crystals.

The holographic readout characteristics were studied with the experimental arrangement shown in Figure 30. The photorefractive grating was written through the interference of the two first order diffracted beams from a Ronchi ruling. This interference pattern resulted in a grating with a 20  $\mu$ m grating

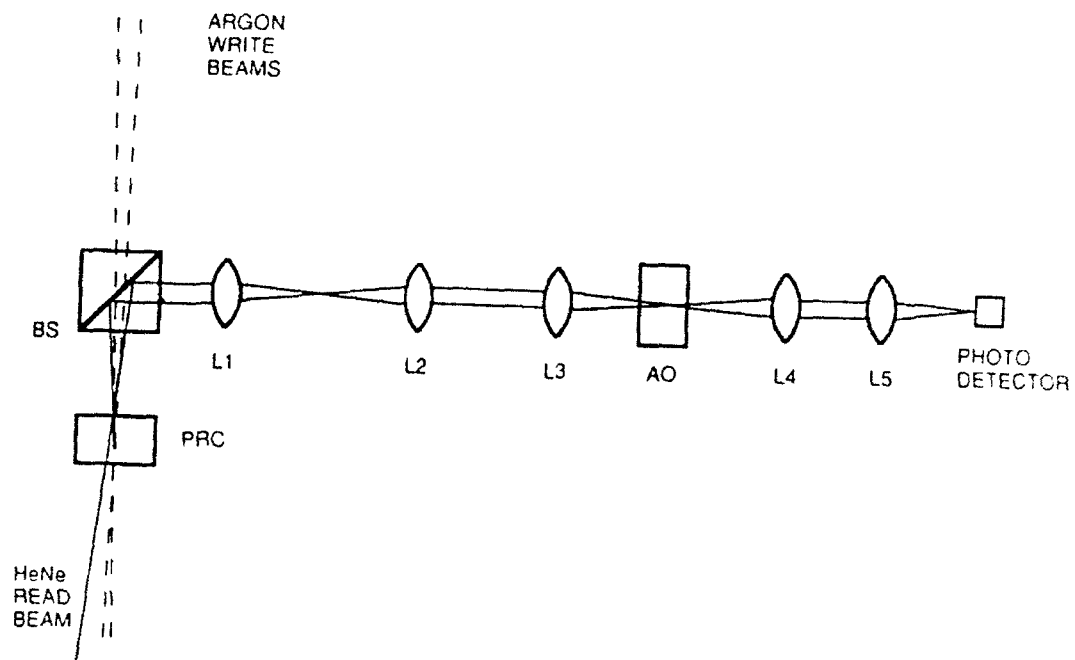


Figure 30. Schematic diagram of layout for holographic readout experiments.

period. A helium neon laser at 632 nm was used as the read beam. A cube beam splitter was used to direct the two read beams (zero and first order beams) through an acousto optic cell for heterodyne read out. Alternately, PD1 could be used to measure the diffraction efficiency or temporal response.

The BSO crystals were 110 cut, and optically polished. Electric fields were applied along the (110) axis direction, and the photorefractive grating was also in this direction. The crystal thicknesses were from 2.5 to 3 mm, and the two other crystal dimensions were for 7 to 10 mm. This (110) configuration produced the maximum diffraction efficiency and minimized two-beam coupling effects.

Experiments were conducted to examine the polarization characteristics. It is important to note that BSO is optically active, with a rotary power of  $21.4^\circ/\text{mm}$  at 632 nm. Because of anisotropic diffraction the maximum diffraction efficiency is obtained with circularly polarized light. For the experimental configuration used, modulation index of  $m = 1$ , a 2.6 mm thick crystal and a square wave electric field of 3.3 KV/cm, the maximum diffraction efficiency was 2%. The diffraction efficiency for linearly polarized light was 1%. This diffraction efficiency was independent of the input polarization.

The heterodyne signal was strongly dependent on the read beam polarization. This is demonstrated in Figure 31. Figure 31a shows an oscilloscope trace of the heterodyne signal for circularly polarized light along with that of the reference rf signal. The noise on the heterodyne signal is due to amplifier noise. Figures 31b and 31c show the signals for two different

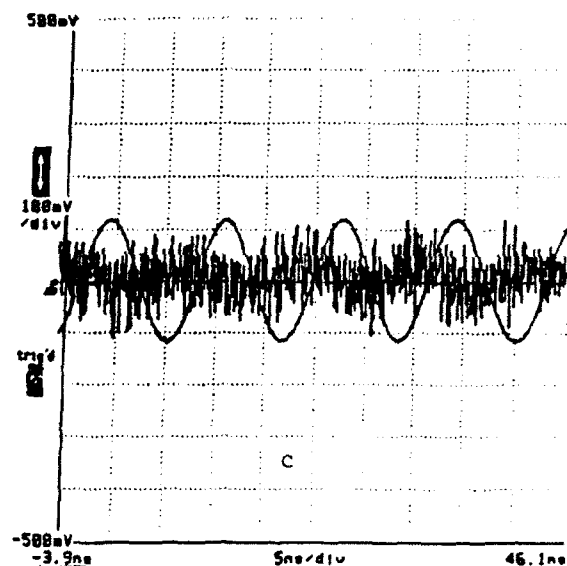
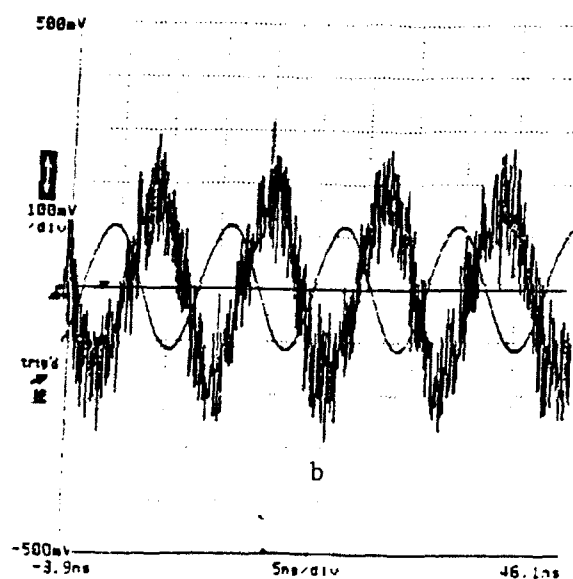
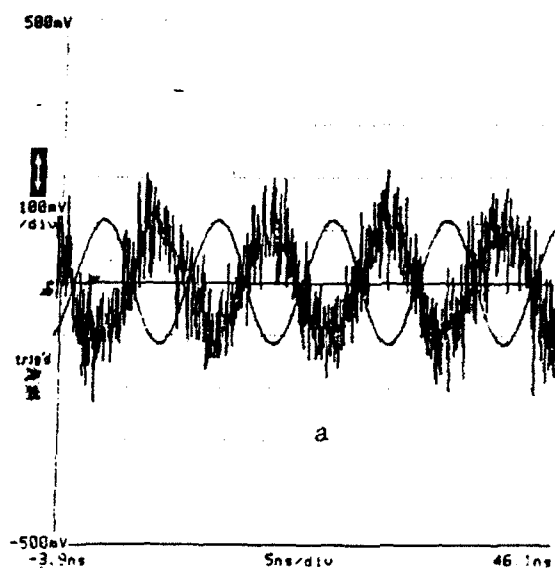


Figure 31. Heterodyne signal in BSO for different read beam polarizations. (a) circularly polarized. (b) linear polarization adjusted for maximum signal. (c) linear polarization adjusted for minimum signal.

linear polarizations which maximize and minimize the heterodyne magnitude. The heterodyne signal for the linearly polarized light is about twice that of the circularly polarized light, even though the diffraction efficiency was only half as great. This polarization dependence can be understood as follows. In addition to being optically active, the polarization of the Bragg diffracted beam is rotated by an angle  $2\psi$ , where  $\psi$  is the angle of the polarization direction of the read beam with respect to the principal electro-optic axis. Therefore the polarization states of the undiffracted and diffracted read beams will not be the same, resulting in a decreased heterodyne efficiency.

#### 4.2 Barium Titanate

Barium titanate was also examined as a candidate photorefractive integrator. The high diffraction efficiency potential, due to the large electro-optic coefficient makes the ferroelectric crystals attractive. The  $\text{BaTiO}_3$  crystal used in this characterization was a (100) cut crystal. The argon write beams were vertically polarized (ordinary polarization) and the HeNe read beam was horizontally polarized (extraordinary polarization). This provided an electro-optic coefficient of 80 pm/V. It should be noted that a much larger electro-optic coefficient can be obtained by a  $45^\circ$  cut crystal. A 2000 V/cm dc electric field was applied along the C-axis direction through silver painted electrodes. Alternating electric fields are not useful in  $\text{BaTiO}_3$ , due to its small  $\mu\tau$  product. A 65% diffraction efficiency was obtained in the 5mm thick crystal under the same illumination conditions as in the BSO experiments. The



heterodyne signal was significantly improved, as the polarization problems experienced in BSO were not present in BaTiO<sub>3</sub>. The photorefractive response time was 160 s for an illumination intensity of 2mW/cm<sup>2</sup>.

## 5. ACOUSTO-OPTIC CORRELATION & APPLICATION

BSO and BaTiO<sub>3</sub> crystals were tested as optical integrators for an acousto-optic correlation application.

### 5.1 photorefractive acousto-optic correlation

The ability of photorefractive crystals to perform the required correlation was experimentally demonstrated for both BSO and BaTiO<sub>3</sub> using the experimental arrangement shown in Figure 32. This configuration combines the time integrating correlation and heterodyne readout. The first order Bragg diffracted output of AO1 ( 200 MHz carrier frequency) was amplitude modulated by  $r(t)$  (40 MHz signal). This signal was correlated with  $s(t)$  (40 MHz) in AO2. The output of AO2 was then imaged in the photorefractive crystal. The integrated correlation signal was read by the heterodyne method, as described above. In this arrangement part of the argon laser beam was split off to provide the read beam. The path difference between the read and write beams was much greater than the coherence length ( $\approx 2\text{cm}$ ). The rf signal  $s(t)$  was also used to provide the input to AO3. The heterodyne output of the photodetector and the rf input were displayed on an oscilloscope. A typical result shown in Figure 33 demonstrates the feasibility of photorefractives in optical signal processing.

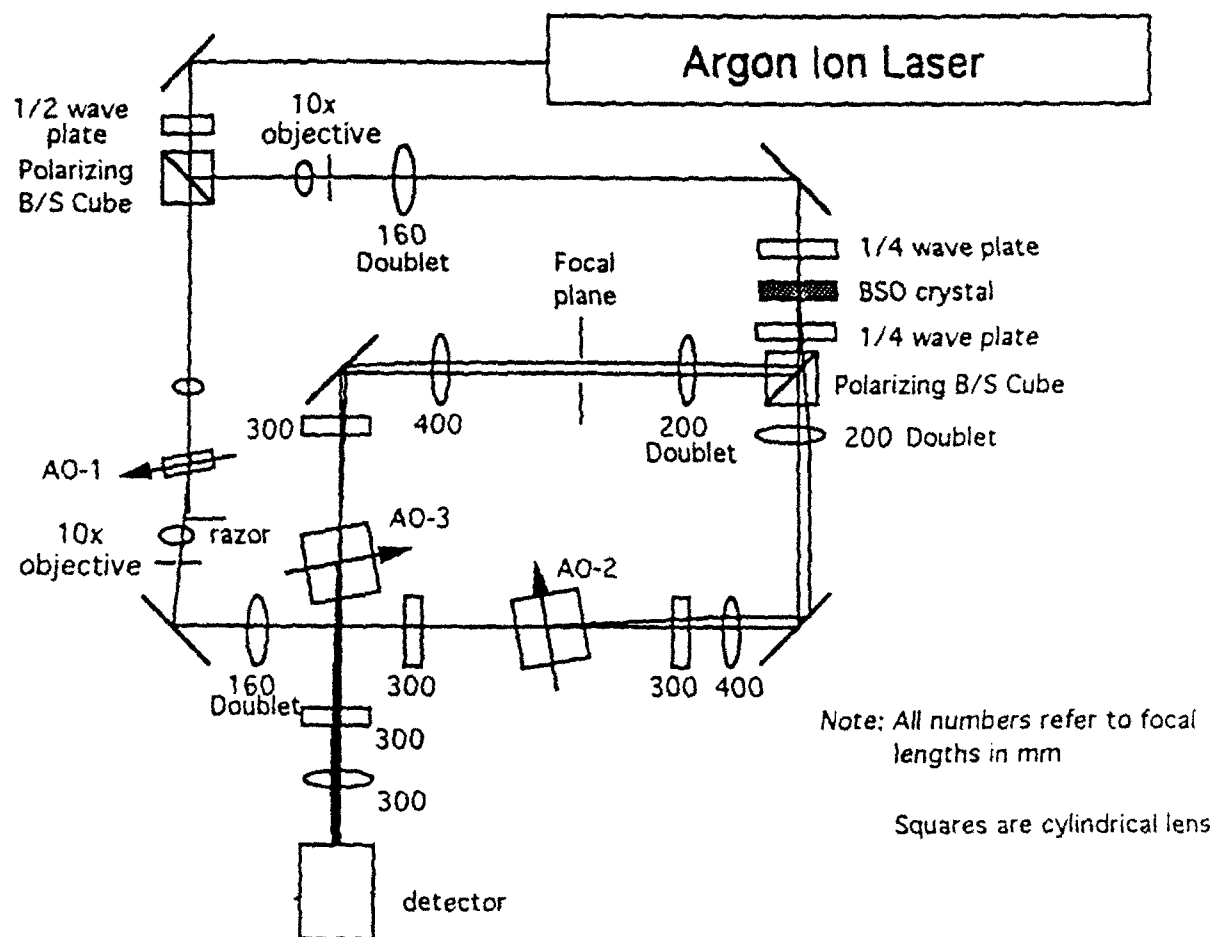


Figure 32. Experimental layout for photorefractive acousto-optic correlation experiments.

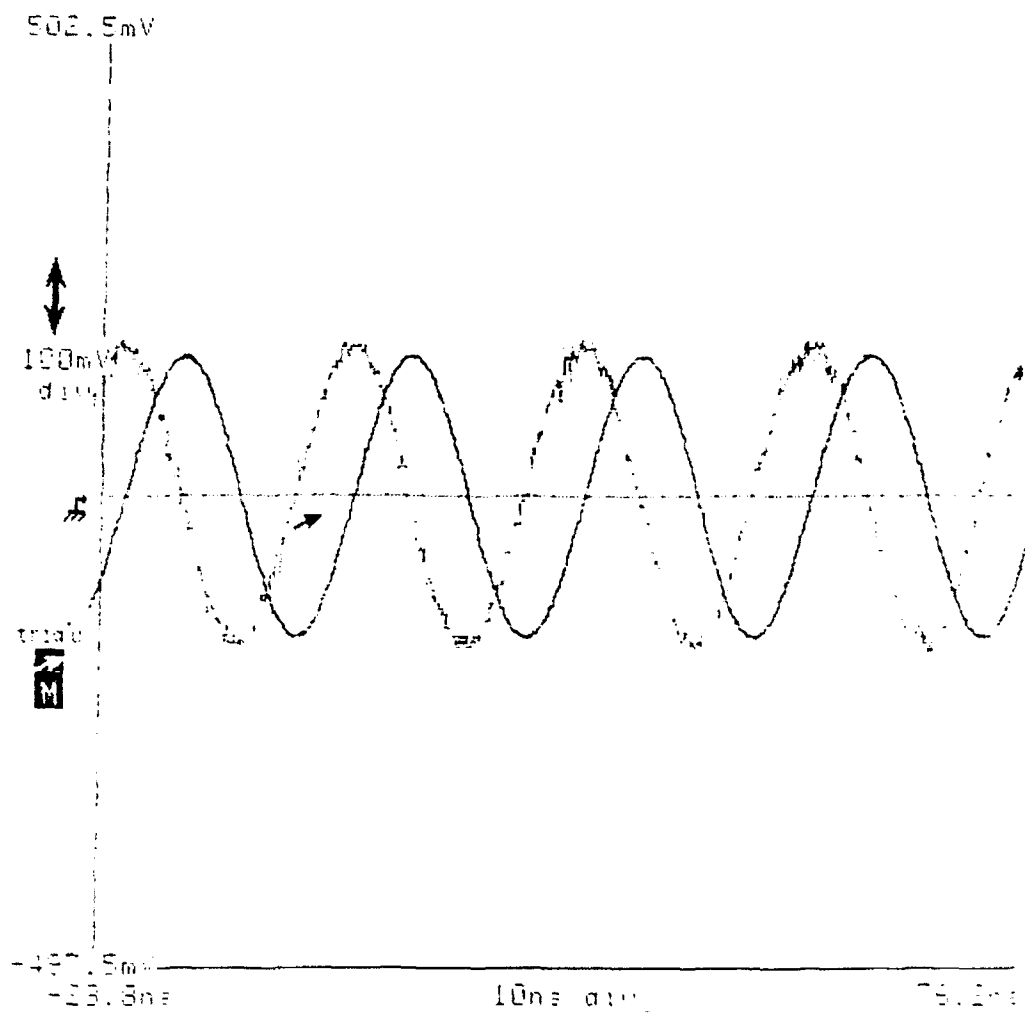


Figure 33. Heterodyne signal of acousto-optic correlation using BSO as an integrating element.

## 5.2 Acousto-Optic Adaptive Processing

The experimental layout shown in Figure 31 can be utilized for an adaptive signal processing application. This processor implements a least mean square algorithm to adaptively cancel a jamming noise introduced into a radar antenna's sidelobes. The acousto-optic adaptive processor concept was developed by General Electric [21]. In their implementation a Hughes liquid crystal light (LCLV) valve was used to perform the integration function. The LCLV was identified as limiting the performance of the processor's performance. The acousto-optic adaptive processor has been modified at Rome Laboratory to include the replacement of the LCLV with a photorefractive integrator. This modification was supported by this effort. In this section the basic concept of the adaptive processor is described and preliminary results of measured performance using a photorefractive integrator are given. Detailed discussion of the acousto-optic adaptive processor design and operation can be found in references 21.

In the adaptive processor, the acousto-optic modulator AO-1 is amplitude modulated by

$$r(t) = r_1(t) + N_o(t) - y(t) \quad (46)$$

where  $r_1(t)$  is the target return signal and  $N_o(t)$  is the jammer noise received by the main antenna, and  $y(t)$  is the signal, determined by the adaptive processor, which is subtracted to cancel out the jammer noise. The acousto-optic cells AO-2 and AO-3 are driven by  $s(t)$  corresponding to the signal from an

auxiliary sidelobe antenna which receives a jammer noise signal that contains multiple delayed versions of the jammer noise. The algorithm finds the correlation between  $r(t)$  and  $s(t)$ , then convolves this result with  $s(t)$  to determine  $y(t)$ . In the optical implementation  $y(t)$  is the heterodyne output of the photodetector.

The cancellation ability of the adaptive processor using photorefractive integrators was demonstrated with BSO and  $\text{BaTiO}_3$ . The optical layout corresponded to that shown in Figure 31, with the output of the photodetector subtracted from the signal used to modulate AO-1. The input signals  $r_1(t)$  and  $s(t)$  were monotone rf signals obtained from the same rf generator. The  $1/4$  wave plates were adjusted to maximize the diffraction efficiency of the BSO photorefractive crystal. For tests with  $\text{BaTiO}_3$  the  $1/4$  waveplates were removed, and the polarizations of the write and read beams were made vertical (ordinary) and horizontal (extraordinary) respectively. Figures 34 and 35 show the cancellation obtained with a BSO crystal using both a dc field and an ac field. A dc field of 8KV/cm was used to obtain 25 dB of cancellation, but accompanied by a large increase in the noise floor. The cancellation with an ac field of 4kV/cm at 1.6 kHz square wave is shown in Figure 35. The cancellation speed of the system was approximately 1 msec.

Figure 36 shows the cancellation obtained with a  $\text{BaTiO}_3$  crystal. Although the cancellation was greater than that obtained with the BSO crystal, the cancellation was not stable. The magnitude of the cancellation jumped around between about 28 dB and about 55 dB. The increased cancellation is attributed to

the higher diffraction efficiency obtained with  $\text{BaTiO}_3$ . The lack of stability is thought to be a consequence of the slow response time.

It should be noted that the adaptive processor cancellation results reported here are considered preliminary. These tests demonstrate proof of principle, and provide information for improved system design. The results demonstrate the tradeoffs between integrator response time and diffraction efficiency.

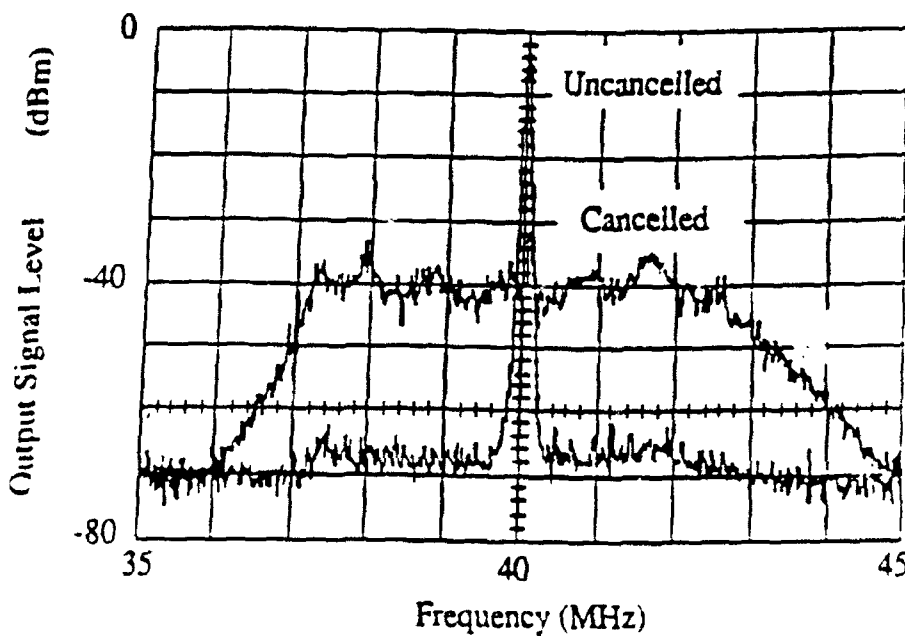


Figure 34. Cancellation performance for BSO with a DC electric field and a monotone rf signal.

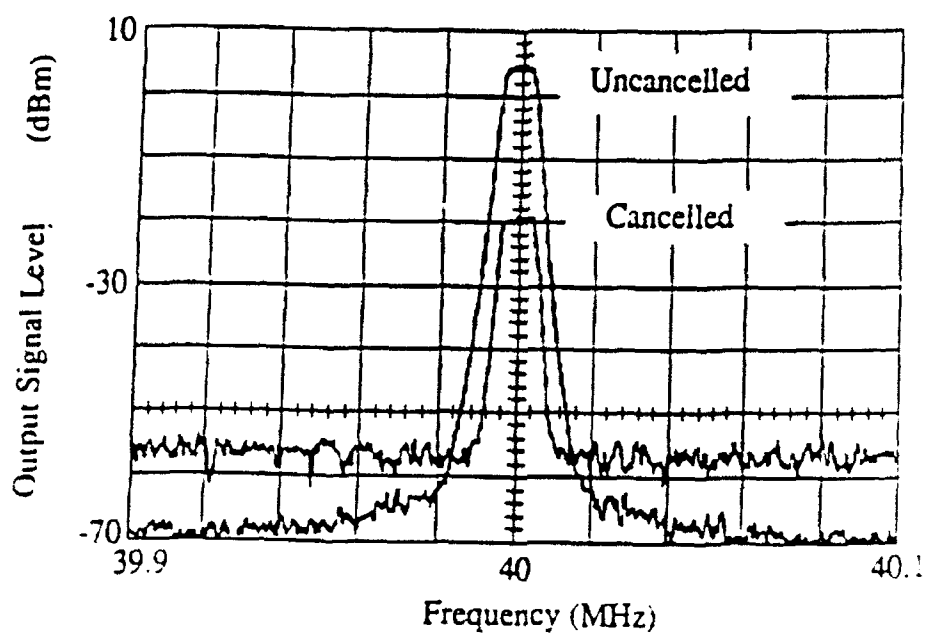


Figure 35. Cancellation performance for BSO with an AC electric field and a monotone rf signal.



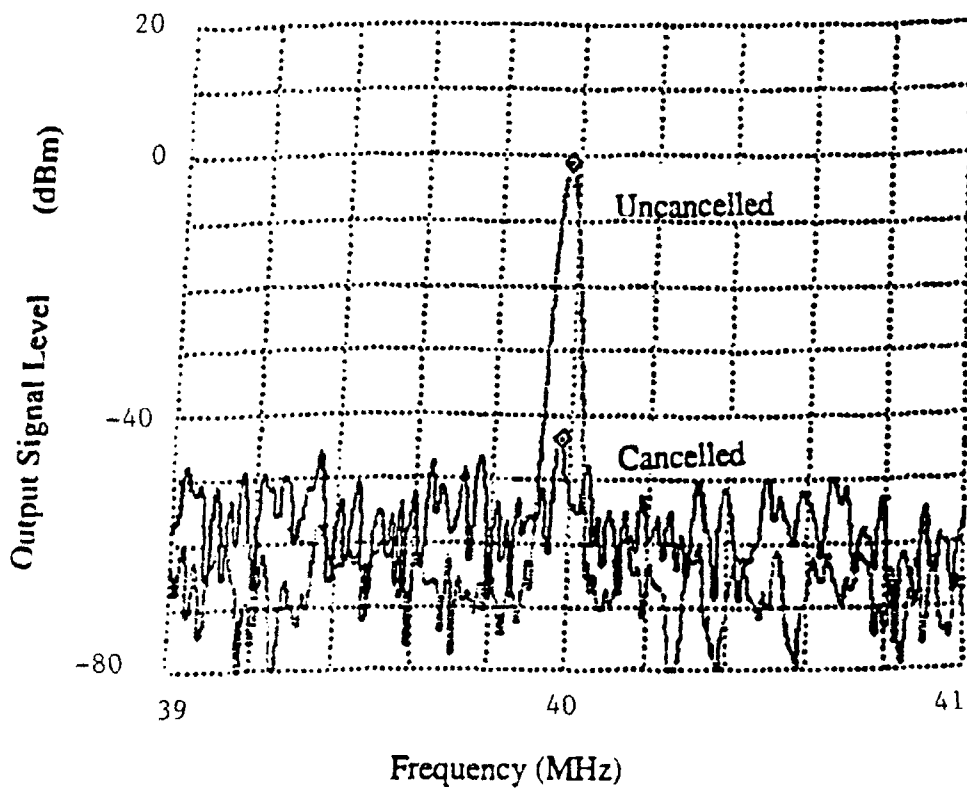


Figure 36. Cancellation obtained using  $\text{BaTiO}_3$  as the photorefractive integrating element in the adaptive processor.

## 6. SUMMARY

The utilization of photorefractive crystals as time integrating elements in an acousto-optic correlation application was investigated.  $\text{Bi}_{12}\text{SiO}_{20}$  (BSO) was examined as a candidate crystal. This choice was based upon speed, size, availability, and wavelength response.

Because of the potential enhancements achievable in BSO, the nonstationary recording techniques of applied ac electric fields and moving gratings were examined in detail. In light of the inadequacies of the small modulation theory, a finite difference technique was developed and used to model the grating formation characteristics. These numerical results provided accurate predictions of the space charge field characteristics. Analytical approximations to the numerical solutions were also determined.

Experiments were conducted with BSO and  $\text{BaTiO}_3$  crystals. BSO provides a fast response time but a small diffraction efficiency due its small electro-optic coefficient.  $\text{BaTiO}_3$  provides a much larger diffraction efficiency, but at the expense of speed. Adaptive processing cancellation was achieved with both crystals. Neither crystal performed exceptionally well alone. The large cancellation obtained with  $\text{BaTiO}_3$  and the good stability observed with BSO demonstrates the feasibility of using photorefractives as integrating elements in acousto-optic adaptive processing.

## REFERENCES

1. D. Psaltis, J. Yu, J. Hong, Appl. Opt. **24**, 3860 (1985).
2. R. Montgomery, SPIE vol 1217, p. 207 (1990).
3. P. Gunter and J.P. Huignard, ed. "Photorefractive Materials and their Applications", Springer Verlag, New York, 1988.
4. M.P. Petrov, S.I. Stepanov, and A.V. Khomenko, "Photorefractive crystals in coherent optical systems", Springer Verlag, New York, 1991.
5. Q.Wang, R.M. Brubaker, D.D. Nolte, and M.R. Melloch, J. Opt. Soc. Am. B **9**, 1626 (1992).
6. A. Partovi, A.M. Glass, D.H. Olson, G.J. Zydzik, H.M. 'Bryan, T.H. Chiu, and W.H. Knox, to be published.
7. P. Refregier, L. Solymar, H. Rajbenbach, and J.P. Huignard, J. Appl. Phys. **58**, 45 (1985).
8. S.I. Stepanov and M.P. Petrov, Optics Comm. **53**, 292 (1985).
9. S.I. Stepanov and M.P. Petrov, Photorefractive materials and their applications I., P. Gunter and J.P. Huignard, ed. Springer-Verlag, New York, 1988).
10. K.Walsh, A.K. Powell, C. Stace, and T.J. Hall, J. Opt. Soc. Am. B **7**, 288 (1990).
11. G.C. Valley, J. Opt. Soc. Am. B **1**, 868 (1984).
12. S.I. Stepanov and S.L. Sochava, Sov. Phys. Tech. Phys. **32**, 1054 (1987).
13. J.E. Millerd, E.M. Garmire, M.B. Klein, B.A. Weschler, F.P. Strohkendl, and G.A. Brost, J. Opt. Soc. Am. B., this issue.
14. G.A. Swinburne, T.J. Hall, and A.K. Powell, IEE 2nd Int. Conference on Holographics, Systems, Components, and Applications, Sept. 1989.

15. L.B. Au and L. Solymar, J. Opt. Soc. Am. A 7, 1554 (1990).
16. L.B. Au and L. Solymar, Opt. Lett., 13, 660 (1988).
17. F. Vachss and L. Hesselink, J. Opt. Soc. Am. B 5, 1814 (1988)
18. M.G. Moharam, T.K. Gaylord, R. Magnusson, and L. Young, J. Appl. Phys., 50, 5642 (1979).
19. A. Marrakchi, J.P. Huignard, and P. Gunter, Appl. Phys. 24, 131, (1981).
20. J.P. Heriau and J.P. Huignard, Appl. Phys. Lett. 49, 1140 (1986).
21. W. Penn, RADC-TR-86-188, (1986).

**MISSION  
OF  
ROME LABORATORY**

*Rome Laboratory plans and executes an interdisciplinary program in research, development, test, and technology transition in support of Air Force Command, Control, Communications and Intelligence (C<sup>3</sup>I) activities for all Air Force platforms. It also executes selected acquisition programs in several areas of expertise. Technical and engineering support within areas of competence is provided to ESD Program Offices (POs) and other ESD elements to perform effective acquisition of C<sup>3</sup>I systems. In addition, Rome Laboratory's technology supports other AFSC Product Divisions, the Air Force user community, and other DOD and non-DOD agencies. Rome Laboratory maintains technical competence and research programs in areas including, but not limited to, communications, command and control, battle management, intelligence information processing, computational sciences and software producibility, wide area surveillance/sensors, signal processing, solid state sciences, photonics, electromagnetic technology, superconductivity, and electronic reliability/maintainability and testability.*